

AD-A144 810

ANALYSIS OF THE FAILURE MECHANISM OF SHIPBOARD  
STRUCTURAL MEMBERS EXPOSED TO FIRE(U) MASSACHUSETTS  
INST OF TECH CAMBRIDGE DEPT OF OCEAN ENGINEERIN.

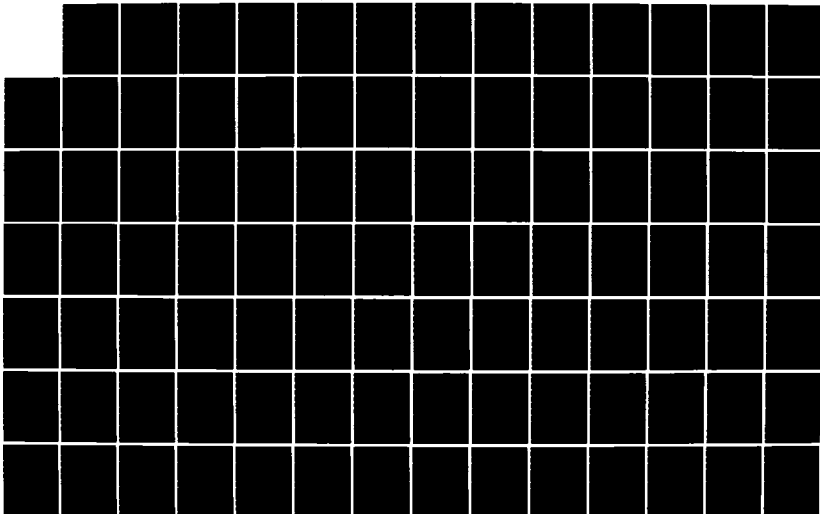
1/2

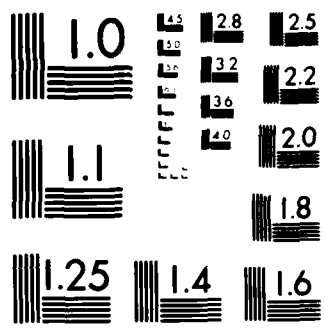
UNCLASSIFIED

R L HIDDENEN JUN 84 N66314-70-A-0013

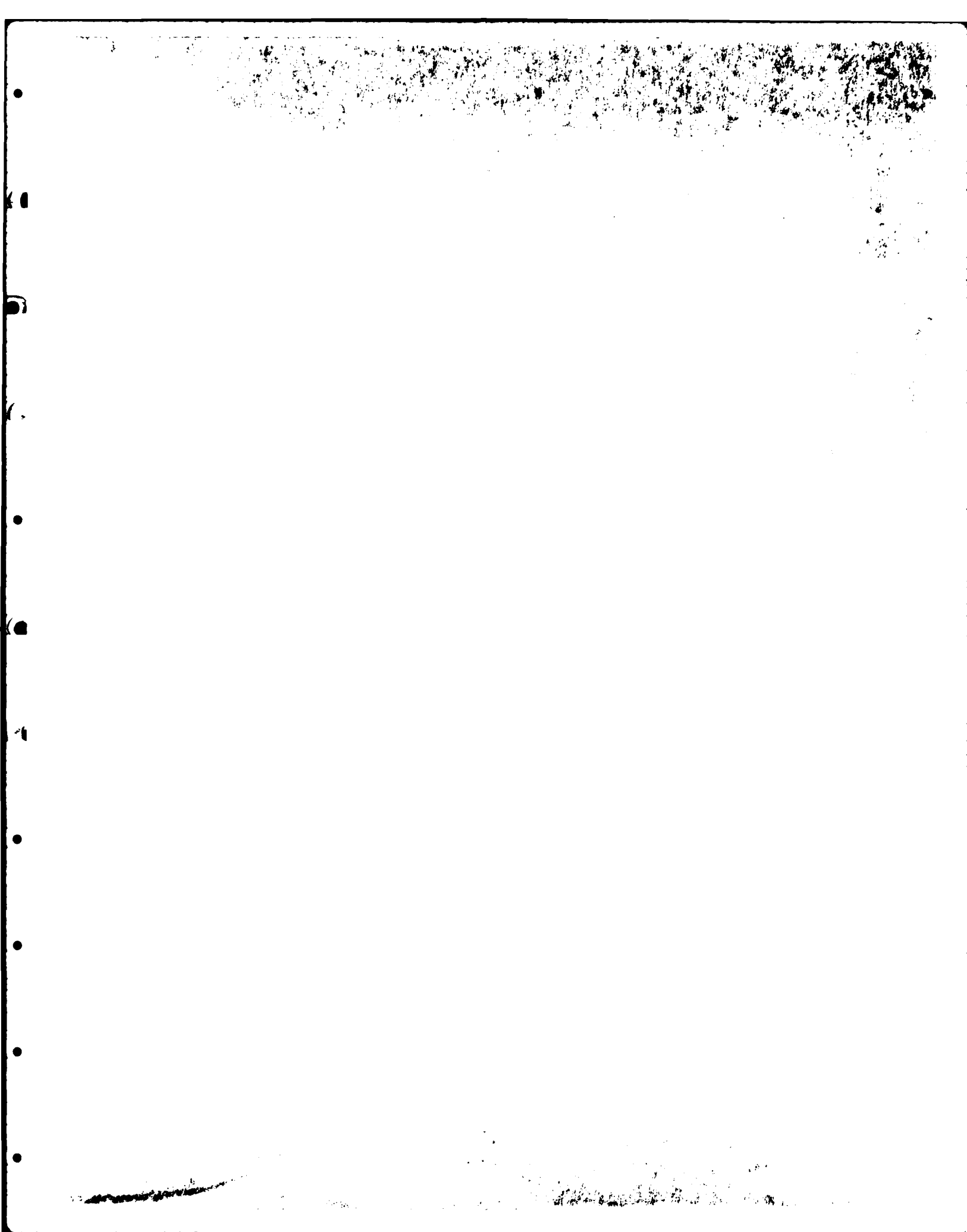
F/G 13/13

NL





MICROCOPY RESOLUTION TEST CHART  
NATIONAL BUREAU OF STANDARDS-1963-A



1  
N66314-70-A-0073

ANALYSIS OF THE FAILURE MECHANISM OF  
SHIPBOARD STRUCTURAL MEMBERS EXPOSED TO FIRE

by

ROBIN LEE HIDDEMEN

B.S. Monmouth College  
1978

Submitted to the Department of  
Ocean Engineering  
in Partial Fulfillment of the  
Requirements of the Degrees of

OCEAN ENGINEER

and

MASTER OF SCIENCE IN NAVAL ARCHITECTURE  
AND MARINE ENGINEERING

at the

MASSACHUSETTS INSTITUTE OF TECHNOLOGY

June 1984

© Massachusetts Institute of Technology

1984

The author hereby grants to the United States Government  
and its agencies permission to reproduce and to distribute  
copies of this thesis document in whole or in part

Signature of Author: Robin Lee Hidemen  
Department of Ocean Engineering  
11 May 1984

Certified by: Tomasz Wierzbicki  
Professor Tomasz Wierzbicki, Ph.D.  
Thesis Supervisor

Accepted by: Alexander Douglas Carmichael  
Professor Alexander Douglas Carmichael, Ph.D.  
Chairman, Ocean Engineering Departmental Committee

This document has been approved  
for public release and sale; its  
distribution is unlimited.

ANALYSIS OF THE FAILURE MECHANISM OF  
SHIPBOARD STRUCTURAL MEMBERS EXPOSED TO FIRE

by

ROBIN LEE HIDDEMEN

Submitted to the Department of Ocean Engineering on 11  
May 1984 in partial fulfillment of the requirements of  
the Degrees of Ocean Engineer and Master of Science in  
Naval Architecture and Marine Engineering

ABSTRACT

The objective of this study is to analyze the behavior of  
a typical ship structural member exposed to fire.

Included in this work are chapters pertaining to the  
modelling of the fire process and the structural member to be  
analyzed. After determining the expected temperature exposure  
of a shipboard structural member, a heat transfer analysis is  
carried out and the resulting load is subsequently used in the  
failure analysis.

The major thrust of this study is the analysis of the  
failure mechanism of the collapse of an I beam. Two methods  
of analysis developed by Kedman, and Hayduk and Wierzbicki,  
are summarized and applied to the case of a fire load. The  
reduced moments due to fire exposure are determined and  
finally recommendations are offered for the use of this  
information in ship structural design.

Thesis Supervisor: Tomasz Wierzbicki  
Title: Professor of  
Applied Mechanics



Accession For	
NTIS GRA&I	<input checked="checked" type="checkbox"/>
DTIC TAB	<input type="checkbox"/>
Unannounced	<input type="checkbox"/>
Justification	<i>form 50 per</i>
By	
Distribution/	
Availability Codes	
Avail and/or	
Dist	Special
<i>A-1</i>	

#### ACKNOWLEDGEMENTS

I would like to acknowledge the invaluable assistance and guidance of my advisor, Professor Tomasz Wierzbicki. Additionally I would like acknowledge my husband, Louis T. Codega for his continued support during my three years at MIT.

## Table of Contents

	Page
Title Page	1
Abstract	2
Acknowledgements	3
List of Figures	6
List of Tables	7
Chapter 1 Introduction	8
Chapter 2 Model of Structure	12
2.1 Background	12
2.2 Load Transmission	13
2.3 Selection of Material	16
Chapter 3 Model of Fire Process	21
3.1 Characteristics of a Shipboard Fire	21
3.2 Development of a Time Temperature Curve	35
Chapter 4 Heat Transfer Analysis	38
4.1 Conduction Heat Transfer	38
4.2 Solution	42
4.3 Results	45
Chapter 5 Analysis of the Failure Mechanism	49
5.1 Kecman's Method	50
5.1.1 Maximum Bending Strength	50
5.1.2 Actual Bending Collapse Mechanism	52
5.1.3 Theoretical Collapse Mechanism	57
5.1.4 Nominal Energy Absorbed During Hinge Rotation	59
5.1.5 The Final Form of the Hinge Moment	64
5.2 Hayduk and Wierzbicki's Method	66
5.2.1 Collapse Modes	67
5.2.1.1 Isometric Transformation Modes	68
5.2.1.2 Hinge Collapse Modes	68
5.2.1.3 Assembled Collapse Modes	70
5.2.2 Analysis	73
5.3 Comparison of Results of the Two Methods	90
Chapter 6 Conclusions and Recommendations	93
6.1 Summary	93
6.2 Recommendations	95

## Table of Contents

	Page
References	97
Appendix A    Heat Transfer Analysis Program	99
Appendix B    Kecman's Analysis Program	101
Appendix C    Hayduk and Wierzbicki's Analysis Program	104



## List of Figures

	Page
1.1 Typical Moment Curvature Relations	10
2.1 Typical Midships Section	14
2.2 Typical Shipboard Structural Beam Elements	15
2.3 Dimensions of Model to be Analyzed	17
2.4 Strength Temperature Relations of ASTM-A36 Steel	20
3.1 Three Periods of Fire	23
3.2 Duration of Full Developed Fires	31
3.3 Average Temperature of Fire Gases for a Typical Compartment	32
3.4 Time Temperature Curves for Various Types of Fire	37
4.1 Fin Configuration	39
4.2 Thermal Conductivity of Plain Carbon Steel	45
4.3 Results of the Heat Transfer Analysis	46
4.4 Dimensions of the Beams Analyzed	47
5.1 Deformation Pattern	53
5.2 Cylindrical Surface TU	55
5.3 Model of Hinge Collapse Mechanism	56
5.4 The Angle of Rotation along GK	61
5.5 Results of Kecman's Analysis	65
5.6 Illustrations of Inextensional and Extensional Deformation Paths	69
5.7 Assembling Folding Modes into More Complicated Patterns	71
5.8 Deformation Patterns	72
5.9 Model of T Section	74
5.10 Folding Mechanisms	75
5.11 Crushing Case	80
5.12 Extensional Collapse Mode - Definition of Geometric Parameters	81
5.13 Bending Case	83
5.14 Definition of the Angle of Rotation	84
5.15 Moment Displacement Relation	85
5.16 Comparison of Approximate and Exact Solutions	87
5.17 Results of Hayduk and Wierzbicki's Analysis	89
5.18 Comparison of the Two Methods	92

## List of Tables

	Page
2.1 Steel Properties	18
3.1 Specific Fire Loading of Shipboard Spaces	25

## Chapter 1

### INTRODUCTION

Traditionally, Marine Engineers have handled the effects of fire on shipboard structures through the use of damage control procedures. Ideally, a structure should be designed to withstand anticipated fire loads. The objective of this work is to apply the methods of post critical analysis of thin-walled structures developed by Mechanical Engineers to analyzing fire loads on board ocean engineering structures, specifically ship structures.

A ship structure is a highly redundant structure. If the load bearing capacity of one member is diminished, then the surrounding structural members carry more of the applied load. Shipboard fires are characteristically highly localized phenomenon which may effect only a small percentage of the entire structure. By examining the effect of fire on a single structural member, one will gain insight into the behavior of the entire structure. Ultimately, ship structures may be designed to withstand the effects of typical shipboard fires.

It is the intent of this study to examine the effect of a

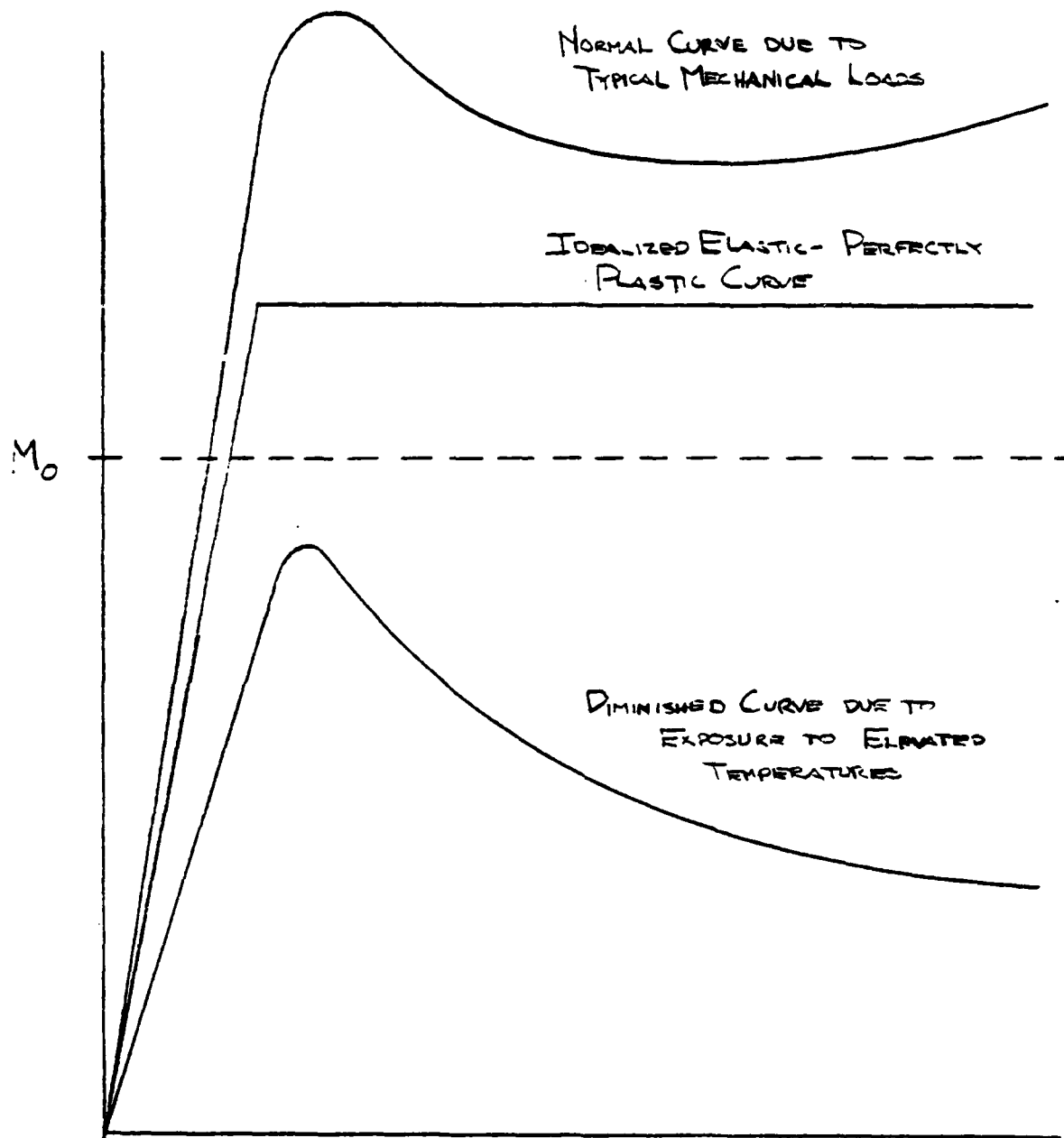
fire on a typical shipboard structure, namely the I beam. The major thrust will be the analysis of the failure mechanism of the beam. Two methods will be introduced which analyze the post yield behavior of an I beam. Figure 1.1 shows graphically how a fire load diminishes the mechanical properties of a beam.

The material yields upon reaching the maximum moment in Figure 1.1. Consider the following relation:

$$\text{Stiffness} = \text{Moment/Curvature.}$$

Beyond the yield point, stiffness is less than or equal to zero. Normally a structural member remains in the elastic range, and the moment remains less than  $M_o$ , the fully plastic yield moment. However, through exposure to fire, the stiffness will decrease so rapidly that the moment will fall below a safe range.

The ultimate objective of this study is to show how much the strength of an I beam is diminished when exposed to fire. To this end, the structure and the fire process will be modelled; and the effect of temperature on the mechanical properties of a selected material will be given. After these models have been developed, a heat transfer analysis will be performed. As a result of this analysis, it will be shown that bending collapse is the primary mechanism of structural



TYPICAL MOMENT CURVATURE RELATIONS

FIGURE 1.1

failure. Next, the failure mechanism analysis methods will be fully developed. Finally, recommendations will be offered for applying the results of this work to the design of an entire ship structure.

## Chapter 2

### MODEL OF STRUCTURE

This chapter will develop the motivation towards choosing an I beam as a typical shipboard structural element. Additionally, a material will be selected; and the temperature dependent properties of that material will be given.

#### 2.1 Background

The principal aspects of ship structural design most commonly employed by Marine Engineers involves the application of rules established by Societies such as the American Bureau of Shipping. These rules are based upon the primary loads experienced by a ship during its lifetime. These loads include: still water bending moments and shearing forces; wave induced moments and shearing forces; impulse loads; thermal loads; and dynamic loads.

These loads which are unique to ocean going vessels are

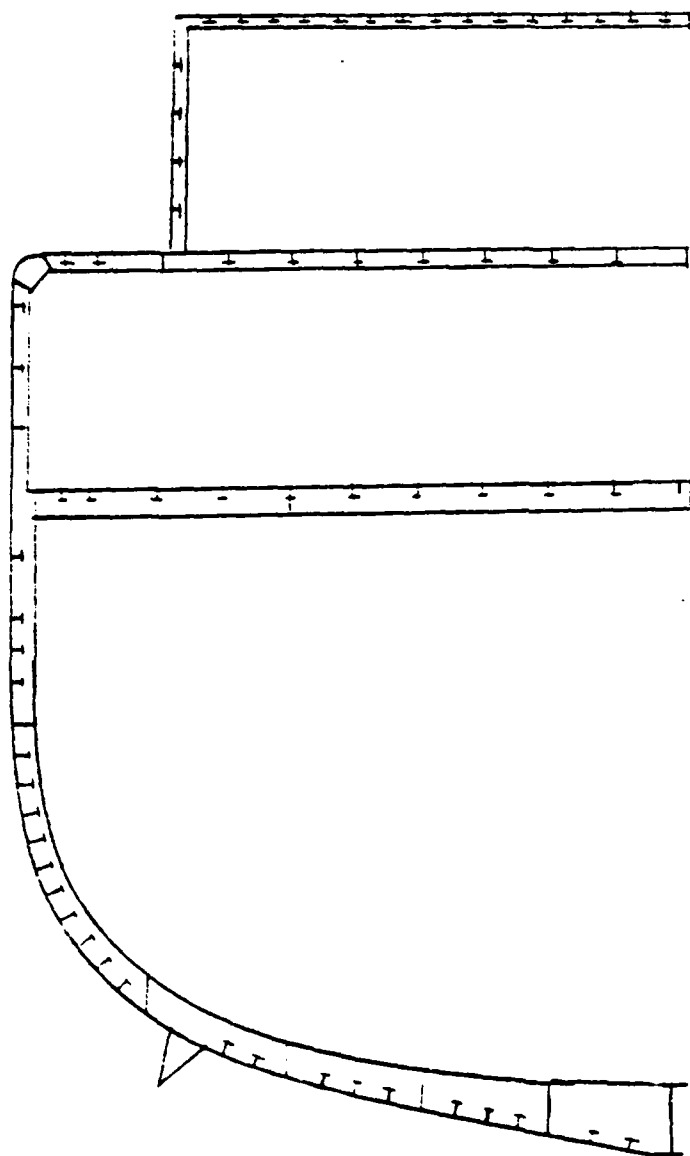
often difficult to accurately predict. Therefore, ship structural design is largely a process involving guesses derived from intuition or empirical data. The primary stress, strain and displacement behavior of the ship structure are due to displacements limited to those parallel to the unloaded midsurface of the plate. Thus, traditionally hull strength is determined through an analysis of the midships section. Figure 2.1 illustrates a typical midships section.

## 2.2 Load Transmission

Today, Ship Structural Engineers have adopted a model which is motivated by considering the loads transmitted to the structure. Loads transmitted to a stiffened plate (by slamming, etc.) are in turn transmitted to the stiffeners and from them to the point supports, and so on. Eventually a load transmitting grillage is derived. Next, boundary conditions will be used to define if the spans are treated as a series of isolated points or continuous beams. In most cases the boundary points will be those which can be described as simple or clamped supports.

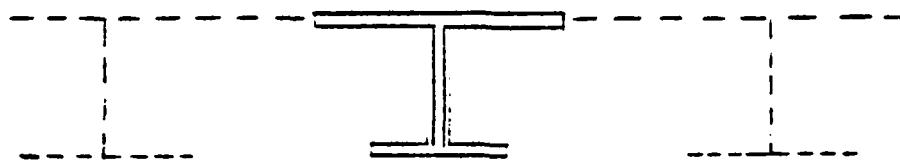
Figure 2.2 shows examples of typical members of a ship's structure. For the purposes of this study, an I beam will be



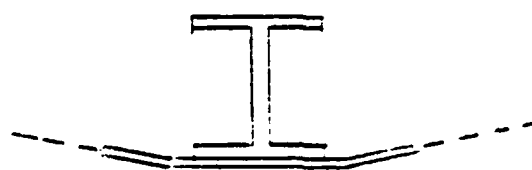


TYPICAL MIDSHIP'S SECTION

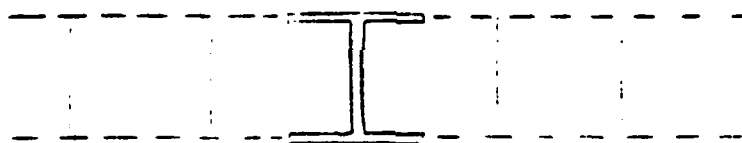
FIGURE 21



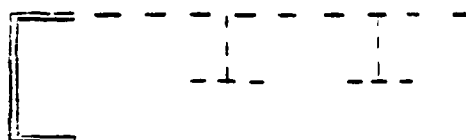
DECK w/ STIFFENERS - UNSYMETRIC H-BEAM



VERTICAL KEEL - I BEAM w/ RAKE



BOTTOM FLOORS - I BEAM



HATCH GIRDER - CHANNEL BEAM

TYPICAL SHIPBOARD STRUCTURAL  
BEAM ELEMENTS

FIGURE 2.2

analyzed as its behavior is considered representative of the open beams in Figure 2.2. Figure 2.3 gives the dimensions of the beam which hereafter will be used as the model to be analyzed.

The first moment of area of the I beam will be required in the analysis.

$$\int_A z dA = t_f (b - t_f) (a - t_w) + \frac{b^2 t_w}{4} \quad (2.1)$$

$A$  = Section Area

$t_f$  = Thickness of the flanges

$t_w$  = Thickness of the web

$a$  = Width of flanges

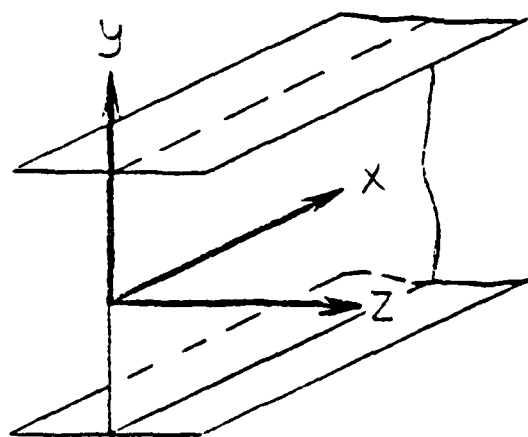
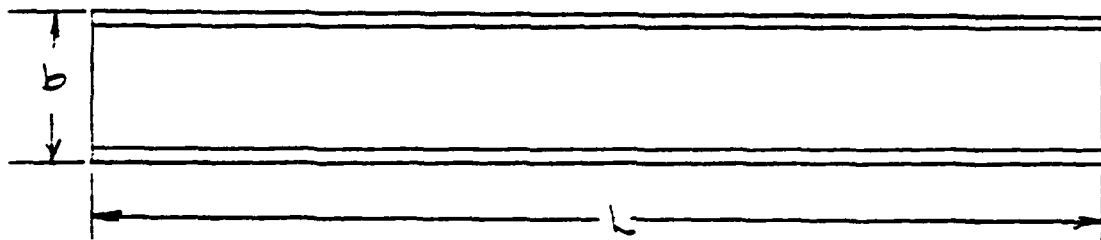
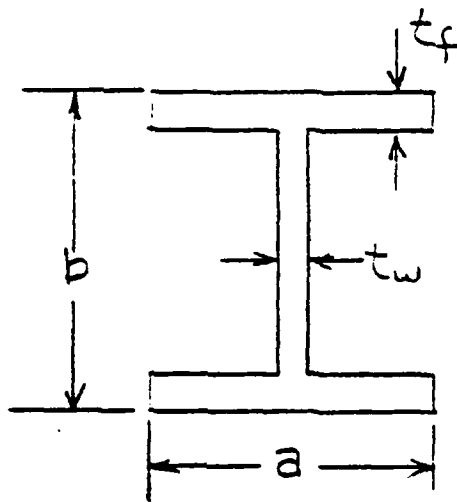
$b$  = Height of web

Assume  $t_w^2$  is negligible. Hence, the first moment of area may be approximated by:

$$\int_A z dA \approx a b t_f + \frac{b^2 t_w}{4} \quad (2.2)$$

### 2.3 Selection of Material

Several materials have been used throughout shipbuilding history starting with wood, and progressing to iron and steel. Today several grades of steel and even titanium are



DIMENSIONS OF MODEL  
TO BE ANALYZED

FIGURE 2.3

used in the shipbuilding industry. One of the most common grades of steels used is ABS Grade A. Material Scientists, however, have not tested ABS Grade A in order to determine the temperature dependent material properties. Ordinary structural steels such as ASTM-A36, have been widely used as a test specimen. Table 2.1 compares the properties of the two steels.

Table 2.1  
Steel Properties

	ASTM-A36	ABS Grade-A
Carbon, max %	0.23	0.26
Phosphorous, max %	0.04	0.04
Sulphur, max %	0.05	0.04
Yield Stress, ksi	36.00	34.00 (min)

It is considered a conservative assumption that an analysis for ASTM-A36 can be used without sacrificing accuracy, (ref. 1).

One of the major contributions to the loss of strength is the temperature dependence of the mechanical properties of the materials under consideration. Several researchers have predicted the deterioration of steel structural elements at elevated temperatures. A search of the literature reveals good agreement among those whom have studied the temperature dependence of material properties.

Harmathy and Stanzak (ref. 2) have carried out several experiments in order to provide to Design Engineers, primarily to those concerned with fire endurance of structural elements, the elevated temperature mechanical properties of common commercial steel products. The temperature dependent expression for Young's Modulus of Elasticity, E, (psi) for ASTM-A36 steel is given here:

$$E = 30 \times 10^6 - 9.3T^2 \quad (2.3)$$

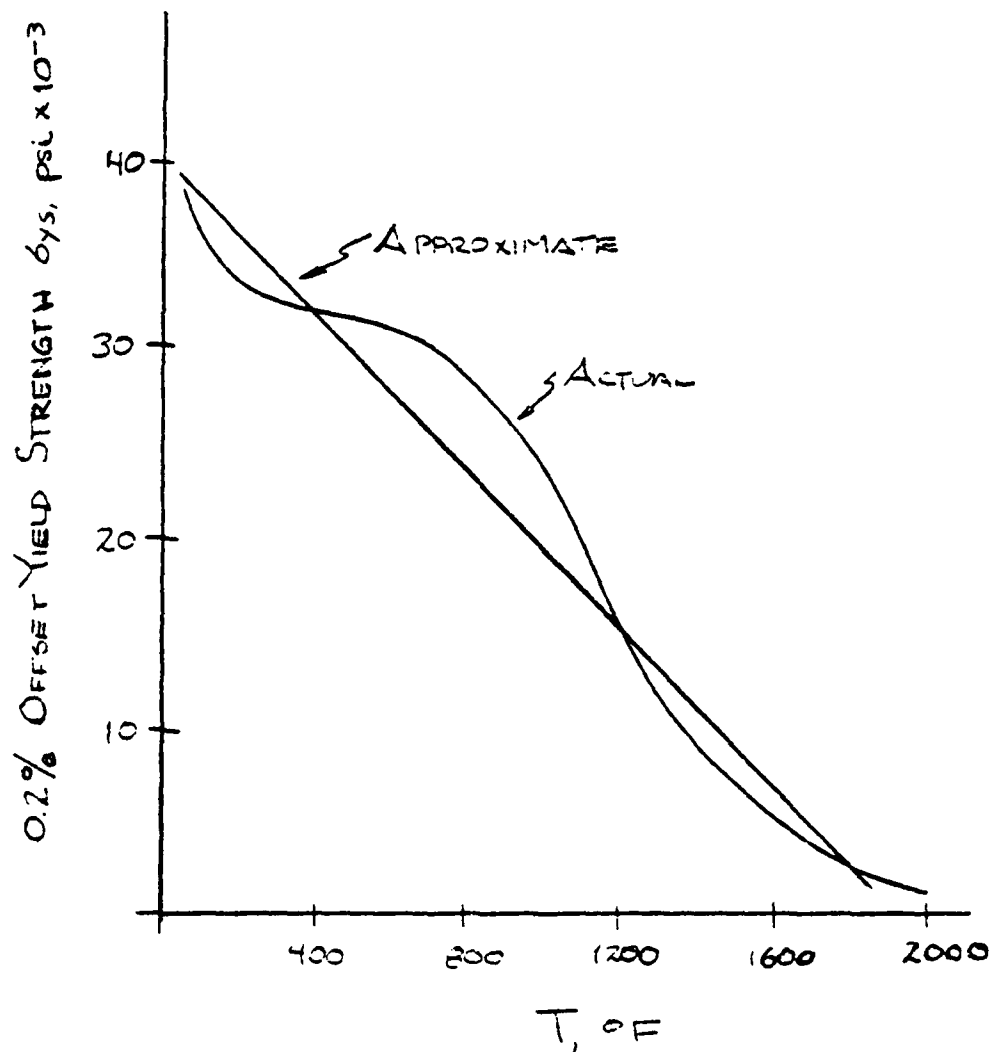
T = Temperature of heat exposure, ° Fahrenheit

Steel loses strength as it is heated. Figure 2.4 illustrates the temperature dependent tensile strength of ASTM-A36 steel.

Notice that between 1000° and 1200° F the tensile strength falls below the usual design stress.

For the purposes of this study, linear dependence of temperature is assumed. The following equation will be used in this analysis.

$$\sigma_o = -20.5T + 40,000.0 \quad (2.4)$$



STRENGTH TEMPERATURE RELATIONS  
OF ASTM-A36 STEEL

FIGURE 2.4

## Chapter 3

### MODEL OF FIRE PROCESS

A survey of the literature reveals several methods of characterizing a fire. Harmathy offers a numerical technique which is summarized in Section 3.1. Most Fire Engineers use a time temperature curve to define the characteristics of a fire. The development of an acceptable time temperature curve is given in Section 3.2.

#### 3.1 Characteristics of a Shipboard Fire

The heat exposure on a shipboard structure resulting from a fire is a function of several identifiable and incidental variables, (ref. 3). The three primary factors contributing to the severity of fully developed fires is the flow rate of air into a burning compartment, (compartment ventilation); the total fire load; and the thermal characteristics of the compartment boundaries.

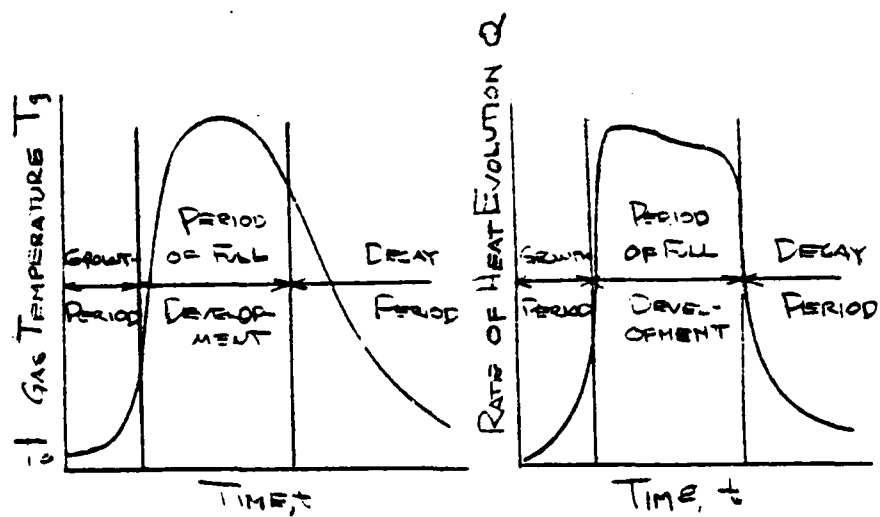


Numerous theoretical studies have determined time-temperature curves of typical fires based on these factors, (ref 3). Even with simplifying assumptions, these factors are only calculable with a computer. Harmathy introduces three easily calculable fire severity parameters which can be assumed to be accurate predictions of the contributing factors to a fully developed fire. These parameters are defined as follows:

1. The duration of the fully developed fire,  $\tau$ ;
2. The overall penetration flux,  $q$ , that is the heat flux absorbed by the compartment boundaries, averaged spatially over the boundary surfaces, and;
3. The average temperature of the compartment gases, (average "fire temperature"),  $T_g$ , averaged spatially over the period of full development.

It is useful at this time to introduce the three periods of freely burning compartment fires. See Figure 3.1. The focus of this study is on the period of full development, since 80-90 percent of the fuel energy is released during this period.

A compartment fire is a fire which is enclosed in a shell of arbitrary shape. Typically on board a ship, ventilation is secured to the compartment with the fire, and free



THREE PERIODS OF FIRE

FIGURE 3.1

communication to the surrounding spaces is not allowed. Fire load is a numerical expression which is a function of the available fuel in the compartment. The units of specific fire load is pounds of wood per square foot, (ref. 1).

To compute the fire load of a particular compartment, the products of the weights in pounds of the material, and the heat capacity are summed for all the combustible materials in the compartment. The resulting expression, which has units of BTU's must be divided by 8000 BTU/lb. This result will provide the same available energy as the equivalent weight of wood.

Equation (3.1) gives the equivalent weight of wood in pounds divided by the deck area of the compartment.

$$F = \frac{\sum_i W_i H_i}{H_w A_F} \quad (3.1)$$

$F$  = Specific fire load, lb/ft<sup>2</sup>

$W_i$  = Weight of individual materials, lb

$H_i$  = Heat capacity of individual materials, BTU/lb

$H_w$  = Heat capacity of wood, BTU/lb

$A_F$  = Area of deck, ft<sup>2</sup>

Table 3.1 gives typical fire load values for various

shipboard compartments, (ref. 4).

Table 3.1

Specific Fire Loading of Shipboard Spaces

	lbs./square feet
Control Spaces	
Wheelhouse/Chartroom	1.5
Fire Control Stations	1.5
Escape Routes	
Corridors	1.5
Stairway Enclosures	1.0
Accommodation Spaces	
Staterooms	
Fire Resistant Furnishings	3.0
Combustible Furnishings	5.0
Public Spaces	
Fire Resistant Furnishings:	
Lounges, Restaurants, etc.	3.0
Ferry Vessels	1.5
Combustible Furnishings	5.0
Sanitary Spaces	0.4
Service Spaces	
Galleys	10.0
Pantry (no heating appliances)	4.0
Food Concession (ferry vessels-	
no combustible stowage)	1.5
Workshops	10.0
Storerooms - Combustibles	10.0
Storerooms - Cleaning gear only	3.0
Ship's Laundry	10.0
Laundry - Private Use	1.5
Main Machinery and Cargo Spaces	10.0
Auxiliary Machinery Spaces	5.0
Tanks and Voids	0.0

It has been determined by several researchers that the flow rate of air into a burning compartment, (ventilation) is just as critical to the severity of the fire as the fire load. The determination of compartment ventilation depends on how the rate of entry of air compares with a critical value. The rate of entry of air into a compartment can be expressed as:

$$U_a = C_1 A_w h_w^{1/2} \quad (3.2)$$

$U_a$  = Flow rate of air, lb/hr

$A_w$  = Area of window, ft<sup>2</sup>

$h_w$  = Height of window, ft

$C_1$  = 240 lb/ft<sup>5/2</sup>-hr

The critical value is defined as:

$$(U_a)_{cr} = C_2 \phi F A_F \quad (3.3)$$

$$C_2 = 28.1 \text{ lb/ft}^2\text{-hr}$$

$\phi$  = Material constant which depends on the furnishings of the compartment. For typical living spaces,

$$0.55 < \phi < 0.90.$$

The air flow factor is expressed as follows:

$$\xi = \frac{U_a}{(U_a)_{cr}} \quad (3.4)$$

Thus, a fire is ventilation controlled if  $\xi < 1.0$ ; and a fire is fuel surface controlled if  $\xi \geq 1.0$ .

The average rate of burning of combustibles,  $R$ , has been determined during the period of full development based upon empirical data. For  $\xi \geq 1.0$

$$R = C_3 \phi F A_F \quad (3.5)$$

$$C_3 = 4.57 \text{ lb/ft}^2\text{-hr}$$

For  $\xi < 1.0$

$$R = 0.163 U_a \quad (3.6)$$

The mass flow rate of gaseous products out of the compartment is:

$$U_g = R + U_a \quad (3.7)$$

It follows that:

$$Q = R(0.932\delta H_1 + 0.068\delta H_2) \quad (3.8)$$

where:

$Q$  = average rate of heat evolution from combustible materials

$H_1$  = ~ 5760 BTU/lb, heat of combustion of char

$H_2$  = ~ 11480 BTU/lb, heat of combustion of volatile decomposition products

$\delta$  = the fraction of heat released by the combustion of the volatile decomposition products inside the compartment

$\delta$  is calculated based upon an estimation of the average flame length,  $l$ :

$$l = C_4 (\phi F A_F)^{1/3} \quad (3.9)$$

$$C_4 = 1.11 \text{ ft}^{1/3}$$

$$l = C_5 U_a^{1/3} \quad (3.10)$$

$$C_5 = 0.366 \text{ ft(h)}^{1/3} / (\text{lb})^{1/3}$$

Then,

$$\text{if } l \leq H_c \quad \delta = 1 \quad (3.11)$$

$$\text{if } l > H_c \quad \delta = (H_c/l)^{1/3} \quad (3.12)$$

where  $H_c$  is the height of the compartment.

The duration of a fully developed fire,  $\tau$ , is calculated as follows:

$$\text{for } \xi \geq 1 \quad \tau = C_6/\phi \quad (3.13)$$

$$C_6 = 0.205 \text{ ft}^2 (\text{hr})/\text{lb}$$

$$\text{for } \xi < 1 \quad \tau = C_6/\phi\xi \quad (3.14)$$

The other two parameters may be obtained numerically from the following equation:

$$q = \frac{1}{A_t} [Q - U_g c_g (\zeta T_g - T_o) - \sigma \frac{A_w}{3} (T_g^4 - T_o^4)] \quad (3.15)$$

where:

$A_t$  = Total area for the compartment

$Q$  = Average rate of heat evolution (BTU/hr)

$C_g$  = Specific heat of compartment gases (BTU/lb-°R)



$T_g$  = Temperature of combustion gases,  $^{\circ}\text{R}$

$T_o$  = Temperature at time = 0,  $^{\circ}\text{R}$

$\sigma$  = Stefan-Boltzman constant,  $0.171 \times 10^{-8} \text{ BTU/ft}^2\text{-hr-}^{\circ}\text{R}^4$

$\zeta$  = Empirical factor, 1.05, dimensionless

$$T_g = \left[ \frac{q}{\sigma \zeta} + (T_o + \frac{q}{k} (2\pi\kappa/\pi)^{1/2})^4 \right]^{1/4} \quad (3.16)$$

where:

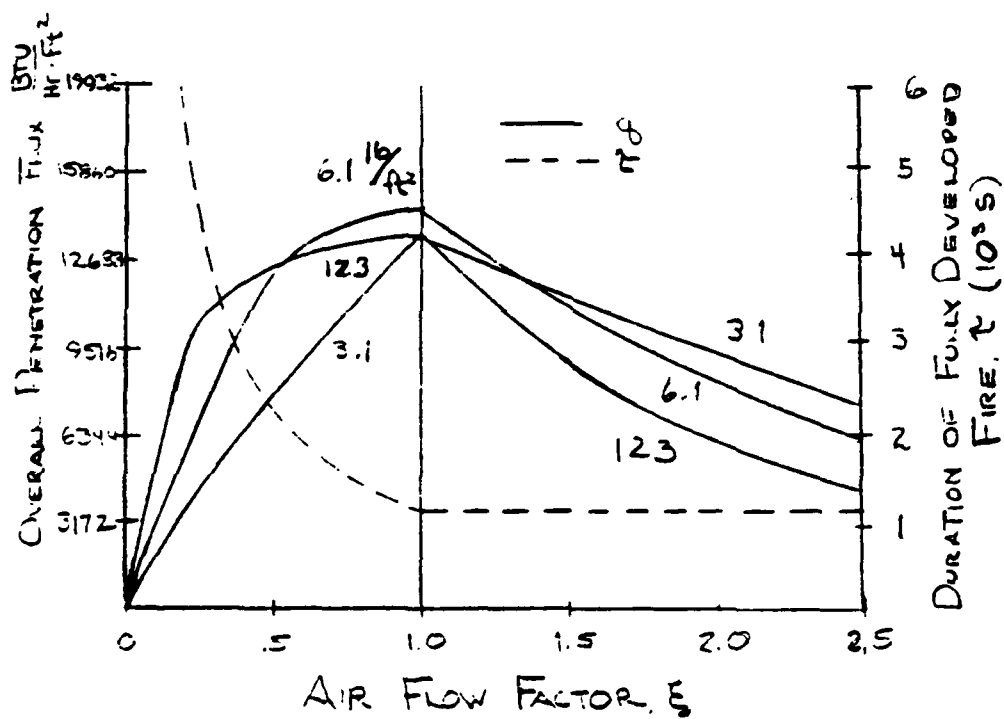
$\eta$  = Empirical factor, 0.9, dimensionless

$\kappa$  = Average thermal diffusivity,  $\text{ft}^2/\text{hr}$

$k$  = Average thermal conductivity,  $\text{BTU/ft-hr-}^{\circ}\text{R}$

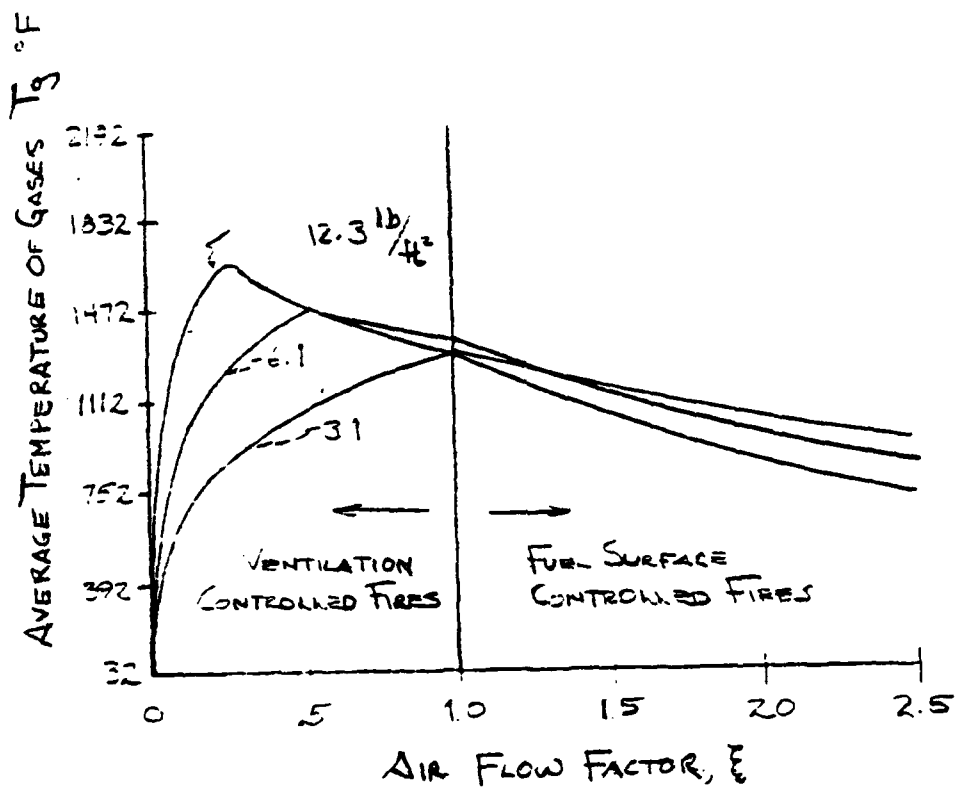
Figures 3.2 and 3.3 show the dependence of the overall penetration flux, and average temperature of gases, respectively, on the air flow factor. These figures were determined empirically for a specific surface of  $0.63 \text{ ft}^2/\text{lb}$ . Curves are given for three values of the specific fire load: 3.1, 6.1, and  $12.3 \text{ lb/ft}^2$ .

Figure 3.2 shows clearly that the maximum penetration flux, and fully developed fire duration occurs at  $\zeta = 1$ . The



DURATION OF FULLY DEVELOPED FIRES

FIGURE 3.2



AVERAGE TEMPERATURE OF FIRE GASES  
FOR A TYPICAL COMPARTMENT

FIGURE 3.3

specific fire loading appears to have little effect on the maximum flux, and the duration is usually quite short. It may also be concluded from Figure 3.3 that the hottest fires occur in ventilation controlled compartments. It is possible at this time to draw some conclusions about shipboard fires. Below decks fires which do not communicate freely with the atmosphere are ventilation controlled. These fires are more destructive as the duration is greater, the average temperature is greater, and the effective heat flux is greater than for an above decks fire.

McCarthy demonstrated the usefulness of Harmathy's technique for predicting fire severity of a typical berthing compartment. Figures 3.2 and 3.3 can be used for a typical berthing compartment, and in accordance with Table 3.1, a specific fire load of  $3.0 \text{ lb/ft}^2$  was used. He assumed that the ventilation is secured, and that one water tight door is open for access to firefighters.

$$A_w = 15.0 \text{ ft}^2$$

$$h_w = 10 \text{ ft}$$

$$U_a = 11384.2 \text{ lb/hr}$$

$$A_F = 150 \text{ ft}^2$$

$$\omega = 0.75$$

$$\frac{[U]}{a_{cr}} = 9483.75$$

$$\zeta = 1.20$$

Hence, the fire is fuel surface controlled. Notice that as  $A_F$  increase the fire approaches ventilation controlled.

From Figures 3.2, and 3.3:

$$\tau = 1.15 \times 10^3 \text{ sec} = 19.2 \text{ min}$$

$$q = 6344 \text{ BTU/hr-ft}^2$$

$$T_g = 1256^\circ \text{ F}$$

It should be appreciated from this discussion that fire is indeed a complex process with several unquantifiable variables. The term destructive potential was introduced in reference 1. The destructive potential of a fire may be considered a function of the maximum temperature obtained, the duration of the fire, the duration of time at maximum temperature, and the quantity of energy transmitted from the fire. Most Fire Engineers use a time temperature curve as a definition of heat exposure. For the purpose of this study, the use of an accepted time-temperature curve will be considered an adequate expression of the fire process.

### 3.2 Development of a Time Temperature Curve

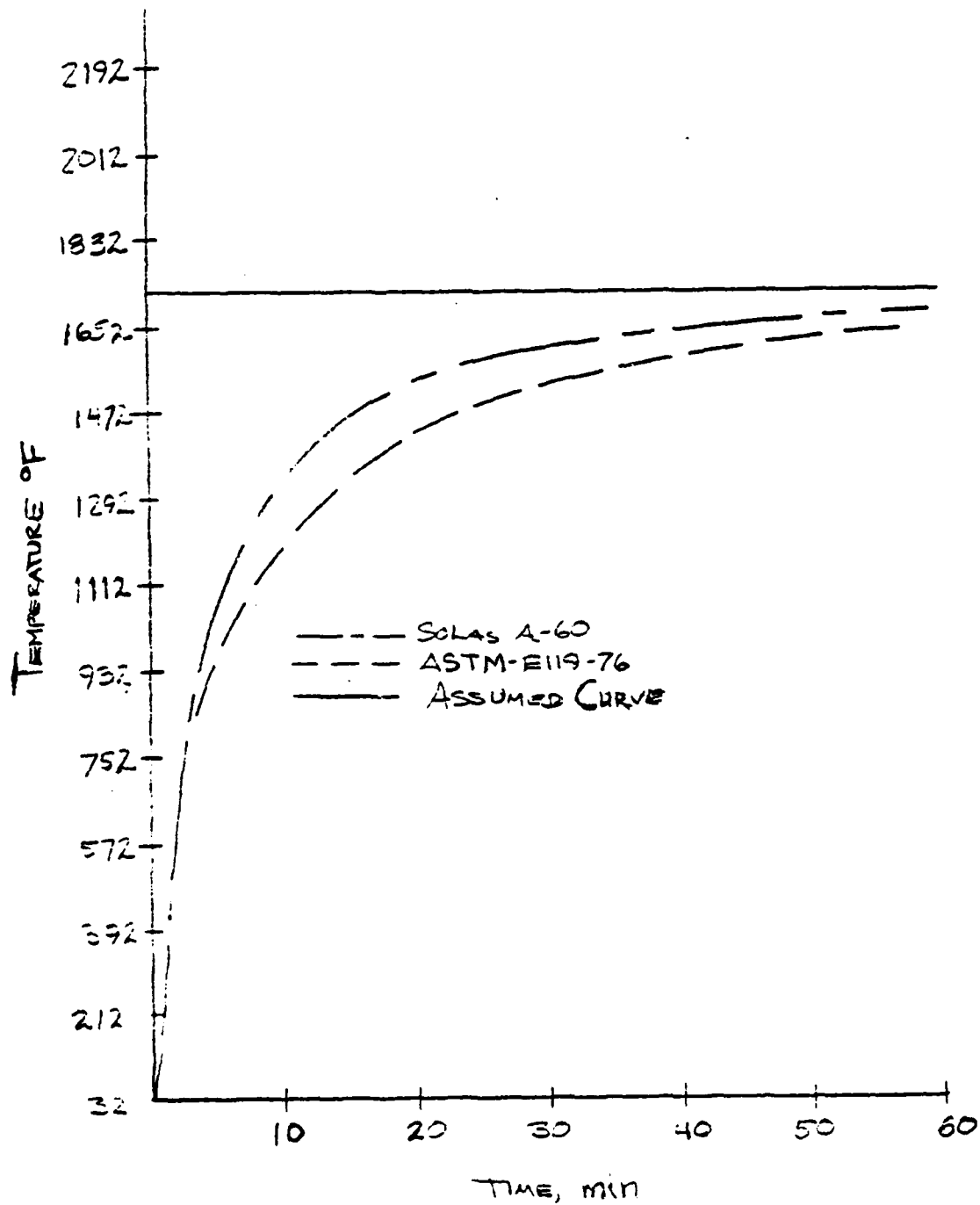
Traditionally, fire tests have been performed based upon prior established standard time temperature curves. The most widely used fire test in this country is the ASTM-E119 which was developed by the American National Standards Institute, (ref. 5). This method was established as a result of the necessity to standardize the structural performance of building construction.

The basic procedure of any fire test is to place the element to be tested into a gas furnace in which the standard time temperature curve is duplicated. The gas temperature is closely monitored through the use of thermocouples. Additionally, deflection, axial thrust, and collapse behavior are measured. The E119 time temperature curve initially rises rapidly reaching 1000<sup>o</sup> F at 5 minutes into the test. Beyond this point, the temperature is increased more slowly so that at the end of one hour the furnace temperature is 1700<sup>o</sup> F. The maximum test temperature, 2300<sup>o</sup> F is reached at 5 hours and held constant thereafter.

Another test method commonly used by Ship Structural

Engineers is the International Convention for the Safety of Life at Sea (SOLAS) A60 test. This test is used for testing non-structural bulkheads from berthing and office compartments. The specimen observed is not loaded but strained at the edges. Other non-structural bulkhead tests are SOLAS A30, A15, A0, B15, B0, but the requirements for these tests are not as severe as for the A60 test, (ref. 1).

For the purposes of this study, reference 6 supports the use of a step change to 1700<sup>0</sup> F vice the gradually increasing temperatures of ASTM-E119 or the SOLAS A60 curves. Figure 3.4 gives the ASTM-E119 curve, the SOLAS A60 curve, and the assumed time temperature relation to be used in this analysis.



TIME/TEMPERATURE CURVE FOR  
VARIOUS TYPES OF FIRES

FIGURE 3.4



## Chapter 4

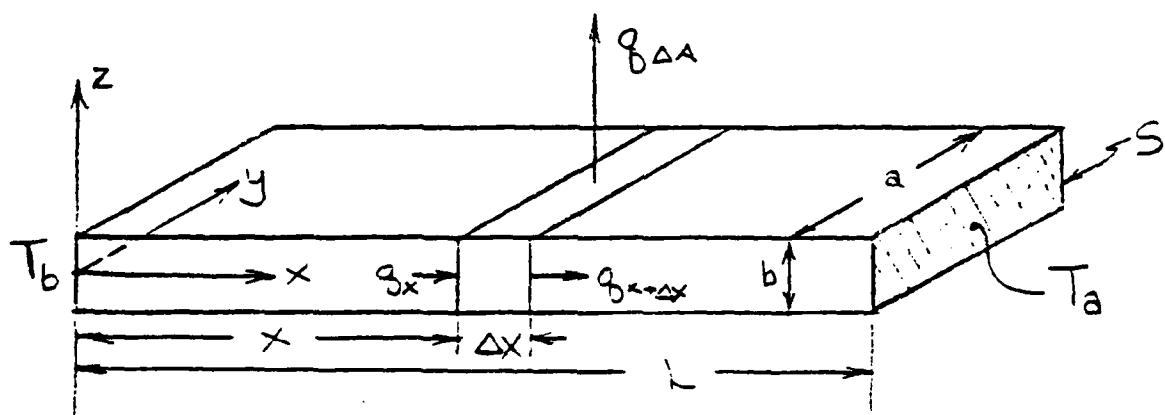
### HEAT TRANSFER ANALYSIS

The intention of this analysis is to determine the relation between temperature and the distance along the length of the beam. A beam exposed to a fire load will be modelled as a fin with a temperature gradient. The temperature at the exposed face is  $T_b$ ; the temperature at the end of the fin is  $T_a$ , the ambient temperature. The geometry of the fin is defined in Figure 4.1

#### 4.1 Conduction Heat Transfer

The following assumptions are used:

- $T_b$  = Temperature at  $x = 0$
- $T_a$  = Temperature at  $x = L$
- The heat transfer is steady state.



FIN CONFIGURATION

FIGURE 4.1

- k = Uniform conductivity of the material,

$$\text{BTU}/[\text{in} \cdot \text{sec} \cdot ^\circ \text{F}]$$

- h = Uniform surface coefficient of heat transfer,

$$\text{BTU}/[\text{hr} \cdot \text{ft}^2 \cdot ^\circ \text{F}].$$

Additionally, this study will use the assumption that the rod is thin, which implies that the temperature in the thin direction, perpendicular to x, is uniform. Therefore, the surface temperature equals the centerline temperature, (ref. 7). Applying an energy balance on an elemental section  $\Delta x$ , yields a governing differential equation. In steady state, with no internal heat generation:

$$q_x = q_{x+\Delta x} + q_{\Delta A} \quad (4.1)$$

Expanding the first term of the right hand side gives the following equation:

$$q_x - q_{x+\Delta x} = q_x - (q_x + \frac{\partial q_x}{\partial x} \Delta x) \quad (4.2)$$

$$q_x - q_{x+\Delta x} = - \frac{\partial q_x}{\partial x} \Delta x \quad (4.3)$$

$$q_x - q_{x+\Delta x} = - \frac{\partial}{\partial x} (-k \Delta y \Delta z \frac{\partial T}{\partial x}) \Delta x \quad (4.4)$$

$$q_x - q_{x+\Delta x} = \frac{\partial}{\partial x} (k S \frac{\partial T}{\partial x}) \Delta x \quad (4.5)$$

Where S = Surface area =  $\Delta y \Delta z$ . Conduction heat transfer across  $\Delta A$  is given in the following

equation:

$$h = \frac{q/A}{T - T_a} \quad (4.6)$$

$$q_{\Delta A} = h(T - T_a)A \quad (4.7)$$

$$q_{\Delta A} = hP\Delta x(T - T_a) \quad (4.8)$$

Where

$P$  = Perimeter =  $2(\Delta y + \Delta z)$

$T$  = Temperature of fin at  $x$

Substituting (4.5) and (4.8) into (4.1) yields:

$$\frac{d}{dx}(kS \frac{\partial T}{\partial x}) \Delta x - hP\Delta x(T - T_a) = 0 \quad (4.9)$$

Finally, the governing differential equation for  $\theta = [T - T_a]$  is:

$$\frac{d^2 \theta}{dx^2} - \frac{hP}{kS} \theta = 0 \quad (4.10)$$

Where  $S$ ,  $k$ , and  $T_a$  are constant.

The differential equation for one dimensional steady state heat flow with one internal heat generation source is:

$$\frac{d^2 \theta}{dx^2} = - \frac{W_i}{k} \quad (4.11)$$

Note that the fin problem is similar to the single internal heat

generation source problem with a negative heat source:

$$W_1 = - \frac{hP\theta}{S} \quad (4.12)$$

#### 4.2 Solution

The method of solution will follow a method provided in reference 8. Assume the solution is of the form given in equation (4.13):

$$\theta = C_1 e^{Bx} + C_2 e^{-Bx} \quad (4.13)$$

Where:

$$B = [hP/kS]^{1/2} \quad (4.14)$$

The boundary conditions for a fin of finite length,  $L$ , as defined by Figure 4.1 are:

$$@ x = 0; \quad \theta = T_b - T_a \equiv \theta_b \quad (4.15)$$

$$@ x = L; \quad \theta = T_a - T_a = 0 \quad (4.16)$$

Substituting (4.15) and (4.16) into (4.13) yields:

$$\theta_b = C_1 + C_2 \quad (4.17)$$

$$0 = C_1 e^{BL} + C_2 e^{-BL} \quad (4.18)$$

Solving for C :  
1

$$C_1 = \frac{-\theta_b e^{-BL}}{e^{BL} - e^{-BL}} \quad (4.19)$$

C follows from (4.17). Finally the solution is:  
2

$$\frac{\theta}{\theta_b} = \frac{e^{B(L-x)} + e^{-B(L-x)}}{e^{BL} - e^{-BL}} \quad (4.20)$$

At this point, it is necessary to solve for B. For the I beam in Figure 2.3, the perimeter to surface area ratio is:

$$\frac{P}{S} = \frac{2(b + 2a - t_w)}{bt_w - 2t_f t_w + 2t_f a} \quad (4.21)$$

Figure 4.2 gives the relation between thermal conductivity and temperature for plain carbon steel, (ref. 9). Within the range of interest,  $70^\circ \text{F} \leq T \leq 2000^\circ \text{F}$ , the curve is considered approximately constant. For the purposes of this analysis, the thermal conductivity at  $1000^\circ \text{F}$  will be assumed.

$$k = 0.0005 \text{ BTU/in sec } ^\circ \text{F} \quad (4.22)$$

The condition of natural convection in a gas is assumed for this analysis, (ref. 7):

$$h = 2.0 \text{ BTU/hr ft}^2 ^\circ \text{F} \quad (4.23)$$

Therefore,

$$B = (P/10.8S)^{1/2} \quad (4.24)$$

where, P/S is given in equation (4.21)

The validity of thin fin theory must now be checked. According to reference 7, the thin fin theory is valid if:

$$\frac{k}{hb} \geq 3 \quad (4.25)$$

Substituting equations (4.22) and (4.23) into (4.25), the maximum value for b is:

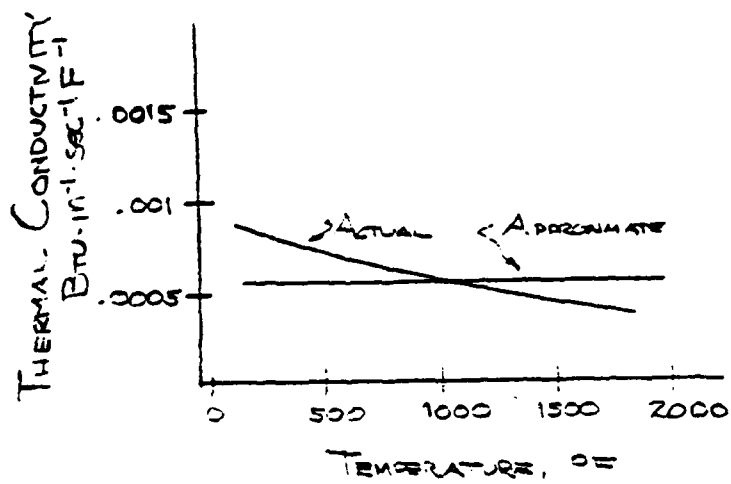
$$b \leq 3.6 \text{ ft} \quad (4.26)$$

This is a reasonable criteria for this study. Therefore thin fin theory is valid.

#### 4.3 Results

It is now possible to draw some conclusions about the heat transfer through the beam. A Microsoft BASIC computer program was written in order to examine several geometric configurations of the beam. The source code for the program is in Appendix A. The results are given graphically in Figure 4.3. The dimensions of the beams examined are in Figure 4.4.

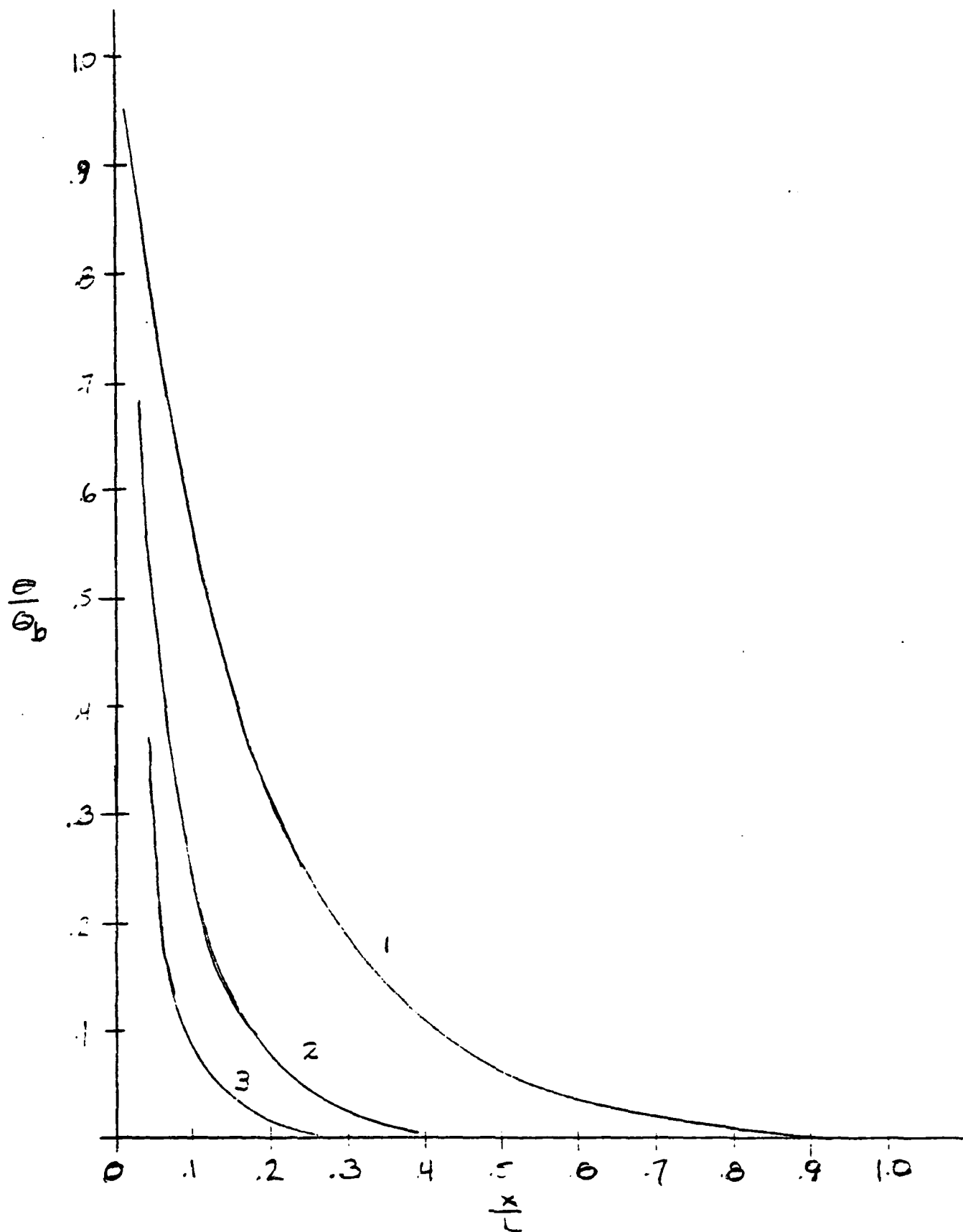
The following conclusion may be drawn from Figure 4.3. As P/S, and L increase, the effect of the fire becomes more localized. With a typical shipboard I beam, the ratio of



THERMAL CONDUCTIVITY OF PLAIN CARBON STEEL

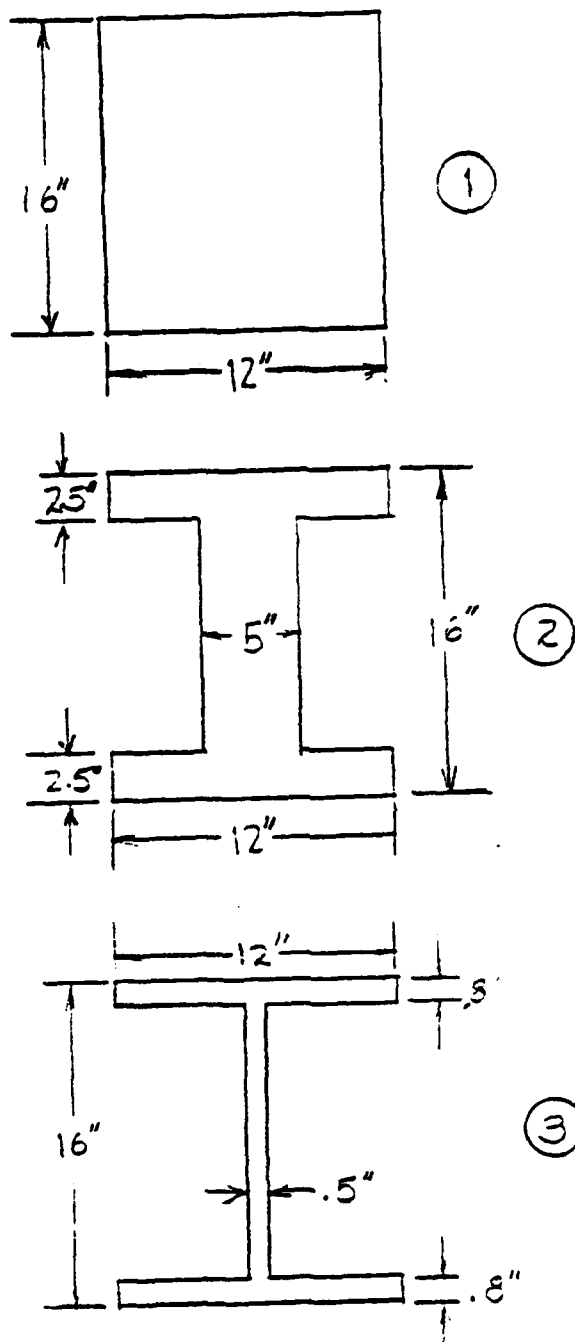
FIGURE 4.2





RESULTS OF HEAT  
TRANSFER ANALYSIS

FIGURE 4.3



DIMENSIONS OF THE  
BEAMS ANALYZED

FIGURE 4.4

perimeter to surface area is such that the fire load may be treated as a point load. That is to say that the heat transfer through an I beam remains highly localized in the vicinity of the fire. All effects of the fire virtually disappear at a distance which is a quarter of the length of the beam away from the fire.

## Chapter 5

### ANALYSIS OF THE FAILURE MECHANISM

As was stated in the preceding chapter, an I beam exposed to a typical shipboard fire will experience the same failure mechanisms as a beam under a point load. Recently there has been increasing interest in this type of failure due to mechanical loads. It is the intention of this study to approximate the shipboard fire load as an additional mechanical load, and to use two of the recently developed techniques for analyzing the failure mechanism. Additionally, this chapter will include summaries of literature which focuses upon bending collapse of thin walled structures.

Kecman (ref. 10) studied the bending collapse behavior of rectangular and square section tubes both theoretically and experimentally. He used a limit analysis technique and a set of formulae to derive the relation between the hinge moment and the associated angle of rotation. Very good agreement was found between his theoretical predictions and the experimental results. His theoretical predictions were in the form of a numerical solution. However, Hayduk and Wierzbicki (ref. 11), gave a closed form analytical solution. In reference 11,

lower and upper bound solutions for the mean crushing strength of cruciforms were obtained by considering bending and extensional modes of deformation.

### 5.1 Kerman's Method

Kecman developed a numerical scheme to analyze the bending collapse of rectangular and square section tubes, (ref. 10). The primary failure mode is local buckling and hinge development. He considered only uniaxial bending collapse.

#### 5.1.1 Maximum Bending Strength

Kecman referred to a study which examined the bending strength of a box shaped section with the webs in tension and the top flange in compression. The effect of the webs was found to be negligible. Therefore, the critical stress of an I beam may be assumed to be the same as the critical stress of a box shape beam.

The critical stress,  $\sigma_{cr}$ , of the section was derived in a

form:

$$\sigma_{cr} = \frac{\pi^2 E}{12(1-\nu)} (5.23 + 0.16 \frac{a}{b}) (\frac{t}{a})^2 \quad (5.1)$$

a = flange width

b = web height

t = web, and flange thickness

If the critical stress is less than the yield stress,  $\sigma_o$  of the material, then the flange buckles. The effective width becomes:

$$a_e = a(0.7 \frac{\sigma_{cr}}{\sigma_o} + 0.3) \quad (5.2)$$

$\sigma_e$  = stress at the edge of the flange

If the critical stress is greater than or equal to the yield stress, then  $a_e = a$ . For the purposes of this study, assume that collapsing occurs when  $\sigma_e = \sigma_o$ . It follows that the maximum moment,  $M_m$ , may be calculated using (5.1) and (5.2).

If  $\sigma_{cr} \leq \sigma_o$ :

$$M_m = \sigma_o t b^2 \frac{2a + b + a_e (3 \frac{a}{b} + 2)}{3(a + b)} \quad (5.3a)$$

If  $\sigma_{cr} > 3\sigma_o$ :

$$M_m = M_o = \sigma_o t [a(b - t) + 0.5(b - 2t)^2] \quad (5.3b)$$

where  $M_o$  = the fully plastic yield moment of the section. If

$\sigma_o < \sigma_{cr} < 3\sigma_o$ , a moment,  $M_o'$ , is defined:

$$M_o' \equiv \sigma_o t b (a + \frac{b}{3}) \quad (5.3c)$$

With the resulting maximum moment:

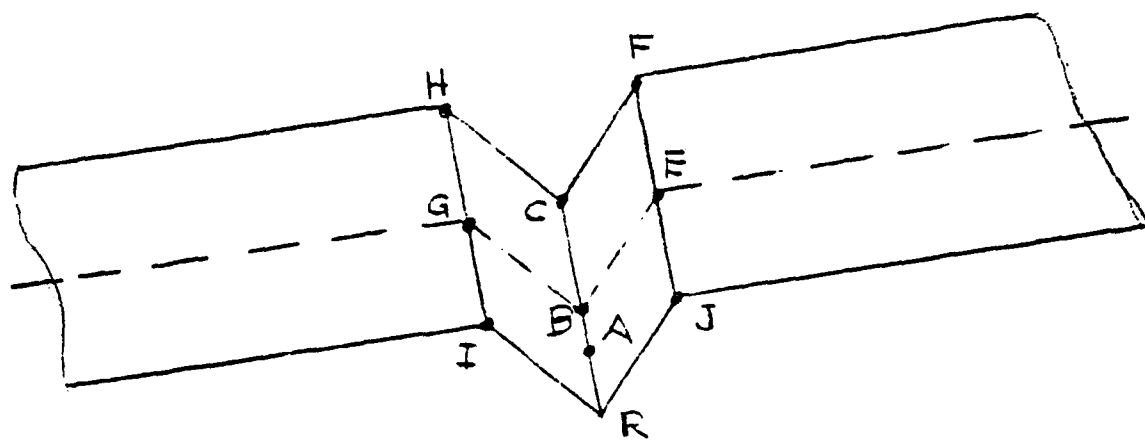
$$M_m = M_o' + (M_o - M_o') \left( \frac{\sigma_{cr} - \sigma_o}{2\sigma_o} \right) \quad (5.3d)$$

### 5.1.2 Actual Bending Collapse Mechanism

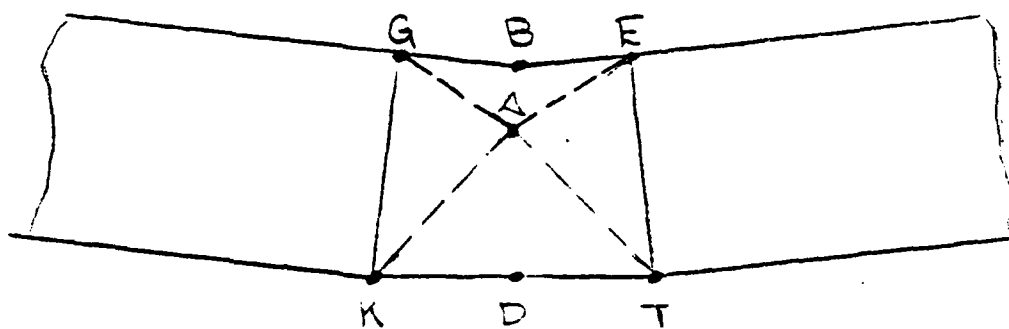
A detailed analysis of the hinge deformation pattern offers insight into the failure mechanism. The deformed pattern is given in Figure 5.1.

The following characteristics of the deformation mechanism were given in reference 10:

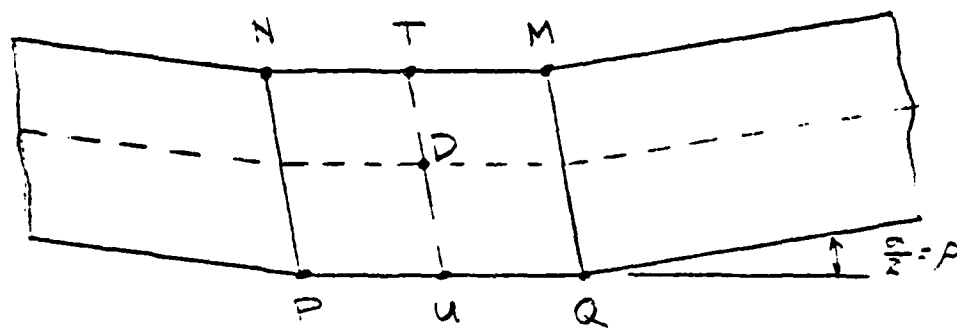
- (a) Most of the plastic deformation is concentrated along the stationary yield lines: JF, HI, EB, GB, FC, HC, CR, BA, GK, and EL.
- (b) Travelling yield lines of rolling deformation were also observed along GA, AE, KA, and LA while the distance BA changes during hinge rotation.
- (c) The corner angle along KL remains almost constant.



TOP FLANGE



WEB



BOTTOM FLANGE

DEFORMATION PATTERN

FIGURE 5.1



(d) The deformation of the tension flange includes the travelling yield lines NP, and MQ, approximately corresponding to the intersection of the undeformed flange planes and the current cylindrical surface TU. See Figures 5.1, and 5.2.

(e) In-plane deformation of the walls was also observed, particularly along the rolling lines GA, AE, BA, HC, CF, IR, and JR. This deformation is essential to maintain hinge kinematics.

(f) The rolling radius,  $r$ , varies slightly along GA, measured by cutting at right angles to GA and its estimated value was approximately proportional to the hinge length.

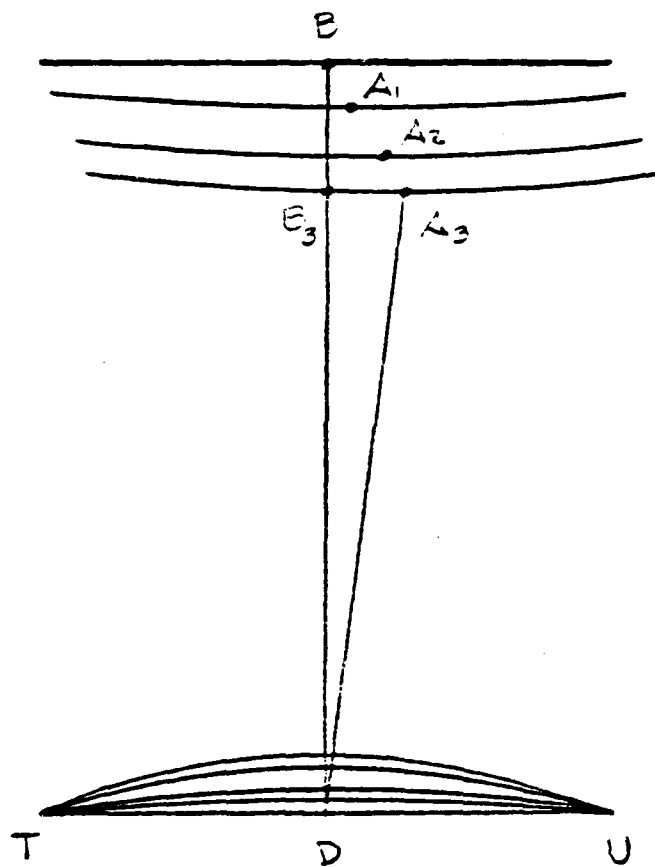
$$r \approx (0.03-0.05) * KL$$

The radius reduces during collapse, so that rolling becomes more and more difficult, until the mechanism jams and starts a new phase of collapse.

(g) The rolling radius along KA, and LA varies from infinity at K and L to a value close to  $r$  in (f) above.

Four distinct phases in the hinge development were identified:

(1) Initial phase with a bulge in the web, A<sub>1</sub>, in Figure



CYLINDRICAL SURFACE  $TU$

FIGURE 3.2



5.3.

(2) Second phase with rolling as described by the cross-section shape  $A_2$  in Figure 5.3.

(3) Third phase indicated by a jamming of the rolling and described by the cross section  $B_3 A_3 D_3$  in Figure 5.3.

(4) Final phase initiated by the contact of the two buckled halves of the compression flange. There is no clear transition from one phase to another.

#### 5.1.3 Theoretical Bending Collapse Mechanism

Since structures most commonly experience hinge collapse described by the second phase which includes rotation angles in the range,  $5-10 \leq \alpha \leq 25-35$ . Kerman based his theoretical analysis on the following assumptions:

- The web and the flanges of the section deform along the concentrated yield lines only;
- The web and flanges are incompressible and inextensible;
- The structural continuity is maintained in two characteristic sections; and

- Some in plane deformation is essential for hinge kinematics.

The model is given in Figure 5.3.

The rolling radius is negligible in comparison with the other hinge dimensions. Points A, B, C, and R are in a straight line. The coordinates of point B are:

$$B(x,y,z) = (h, b \cos \rho - [b \sin \rho (2h - b \sin \rho)]^{1/2}, 0) \quad (5.4)$$

From continuity of the middle section, the web height, b, is determined:

$$b = z_A + (y_A^2 + z_A^2)^{1/2} \quad (5.5)$$

With  $y_B = y_A$ , and equations (5.4), and (5.5):

$$z_A = b \sin^2 \rho - h \sin \rho + [b \sin \rho (2h - b \sin \rho)]^{1/2} \cos \rho \quad (5.6)$$

An analysis of the rotation of the fiber in the top flange will lead to the equation for the hinge length, 2h. For a fiber which is initially parallel to the beam and passes through point A, longitudinal continuity is implied. The distance from this fiber and the edge KL is  $AD = b - z_A$ .

Initially, the coordinates of the fiber and the line GK are  $[0, b - z_A, 0]$ . After rotation, the coordinates are  $[(b - z_A) \sin \rho, (b - z_A) \cos \rho, 0]$ . Point A has the coordinates  $[h, y_A, z_A]$ .

z 1. The distance from point A and the rotated point is h if the web and flanges are inextensible. The equation for h is therefore:

$$h^2 = [h - (b - z_A) \sin \rho]^2 + [y_A - (b - z_A) \cos \rho]^2 + z_A^2 \quad (5.7)$$

Substitution of (5.4), and (5.6) into (5.7); and meeting the condition required by (5.5), it may be said for any ratio a/b, and any rotation angle:

$$2h = a \quad \text{or} \quad 2h = b \quad (5.8)$$

The value which yields the lowest energy absorption will be used. Thus,

$$\begin{aligned} 2h &= a & \text{if } a &\leq b \\ 2h &= b & \text{if } b &\leq a \end{aligned} \quad (5.9)$$

The second phase of deformation is complete when the rotation angle equals the jamming angle,  $\alpha_J$ . Jamming starts when the two buckled halves of the compression flange contact each other. From Figure 5.3 the jamming angle is:

$$\alpha_J = 2 \arcsin \rho \left( \frac{h - 0.5t}{b} \right) \quad (5.10)$$

#### 5.1.4 Nominal Energy Absorbed During Hinge Rotation

The assumptions listed in the previous subsection imply

that all the energy is plastic and is absorbed along the yield lines of the theoretical collapse mechanisms. Relative rotation along the flange edges JF, and IH results from hinge rotation, see Figure 5.1. From geometry, of Figure 5.3:

$$\gamma = \frac{\pi}{2} - \rho - \arcsin(1 - \frac{b}{h}\sin\rho) \quad (5.11)$$

The energy absorbed along these edges becomes:

$$W_1 = W_{JF} + W_{IH} = 2m_p a [\frac{\pi}{2} - \rho - \arcsin(1 - \frac{b}{h}\sin\rho)] \quad (5.12)$$

$m_p$  = Average fully plastic moment of a unit width of  
the flange

Similarly, it may be said:

$$W_2 = W_{CR} = m_p a [\pi - 2\arcsin(1 - \frac{b}{h}\sin\rho)] \quad (5.13)$$

The energy absorbed by the yield line AB can be found from (5.11), where the length of  $AB = z_A$  is known from (5.6),

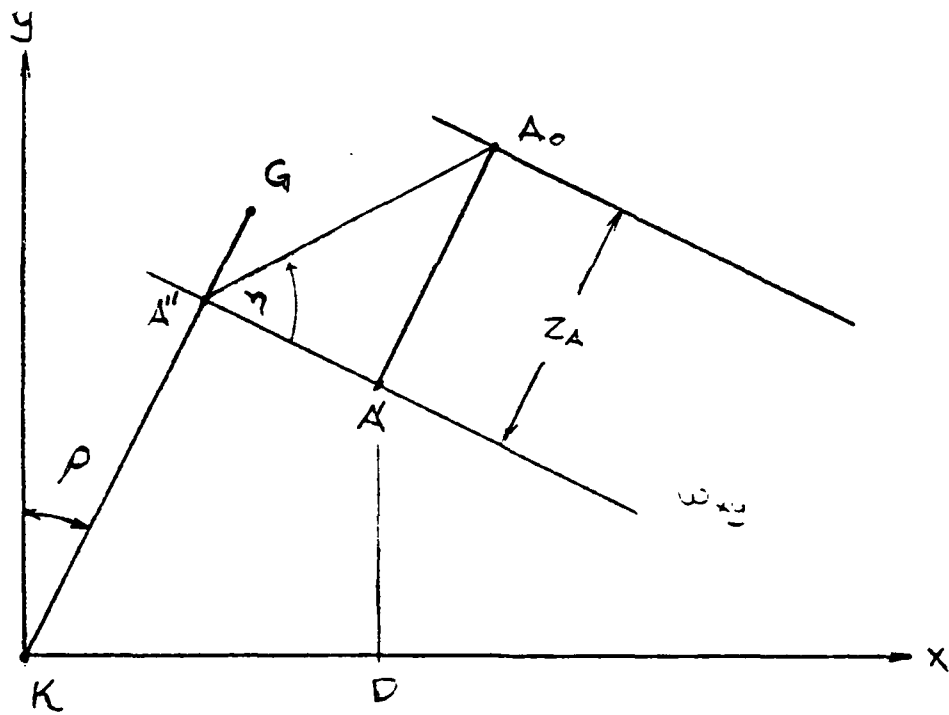
and the relative rotation is  $(\pi - 2\beta)$ . Hence:

$$W_3 = W_{AB} = m_p [b\sin^2\rho - h\sin\rho + (b\sin\rho(2h - b\sin\rho))^{1/2} \cdot \cos\rho] [\pi - 2\arcsin(1 - \frac{b}{h}\sin\rho)]$$

Similarly, along BG, the length is h, and the relative rotation is  $\pi/2$ :

$$W_4 = W_{BG} + W_{BE} = m_p h\pi \quad (5.15)$$

Figure 5.4 shows the relative rotation,  $\eta$ , along yield



THE ANGLE OF ROTATION,  
 $\gamma$  ALONG GK

FIGURE 5.4



line GK. The construction of this figure is detailed as follows: the plane  $\omega_{xy}$  is normal to GK and contains point A.

Point A' is the projection of A onto the xy plane. A<sub>0</sub> is

obtained by rotating  $\omega$  about its intersection  $\omega_{xy}$  with the xy

plane. Coordinates of A'' are:

$$y_{A''} = \frac{h \tan \rho + b \cos \rho - [b \sin \rho (2h - b \sin \rho)]^{1/2}}{1 + \tan^2 \rho} \quad (5.16)$$

$$x_{A''} = y_{A''} \tan \rho \quad (5.17)$$

The energy absorbed along both the GK, and EL lines are then:

$$W_5 = W_{GK} + W_{EL} = 2m_p \arctan \left[ \frac{z_A}{[(h - x_{A''})^2 + (y_{A''} - y_B)^2]^{1/2}} \right] \quad (5.18)$$

The rolling radius along the yield lines GA, and AE remains relatively constant, so:

$$W_6 = W_{GA} + W_{AE} = 2m_p \left( \frac{h}{r} \right) z_A \quad (5.19)$$

During hinge rotation, the rolling radius varies as described by:

$$r = (0.07 - \frac{\alpha}{70})h \quad (5.20)$$

Equation (5.20) is based on empirical data. Kecman approximated the variation of the rolling radius along KA with a hyperbolic approximation:

$$r_{KA} = \frac{KA}{l_K} \quad (5.21)$$

Where  $l_K$  is the distance from K along KA. The linear variation of the rolled length between K and A is given by:

$$l_r = \frac{l_K}{KA} z_A \quad (5.22)$$

The energy along KA is:

$$W_{KA} = \frac{2m z_A KA}{3r} \quad (5.23)$$

or

$$W_7 = W_{KA} + W_{LA} = \frac{4}{3} m \frac{z_A}{p r} [h^2 + y_B^2 + z_A^2]^{1/2} \quad (5.24)$$

The relative rotation along yield lines PN, and QM is  $\rho$ , whereas along KL, and MN the angle is given by:

$$\xi = \arctan\left(\frac{z_A}{y_A}\right)$$

Finally, the energy absorbed by these yield lines is approximated by:

$$W_8 = W_{PN} + W_{QM} + W_{KL} + W_{MN} = 2m_p \left[ ap + 2h \arctan\left(\frac{z_A}{y_A}\right) \right] \quad (5.25)$$

At this point, the total energy absorbed by the hinge may be expressed as:

$$W(\alpha) = \sum_{i=1}^8 W_i(\alpha) \quad (5.26)$$

This result is valid for a rotational angle less than the jamming angle. Kecman determines the moment-angle

relationship numerically from the following equation:

$$M(\alpha) = \frac{W(\alpha + \Delta\alpha) - W(\alpha)}{\Delta\alpha} \quad (5.27)$$

Where  $\Delta\alpha$  represents a small but finite increment of the hinge angle,  $\alpha$ .

This formulation assumes that the material is ductile enough not to fracture during hinge rotation or subsequent bending collapse. This is considered a safe assumption for common structural steels. The average plastic moment is given by the following equation:

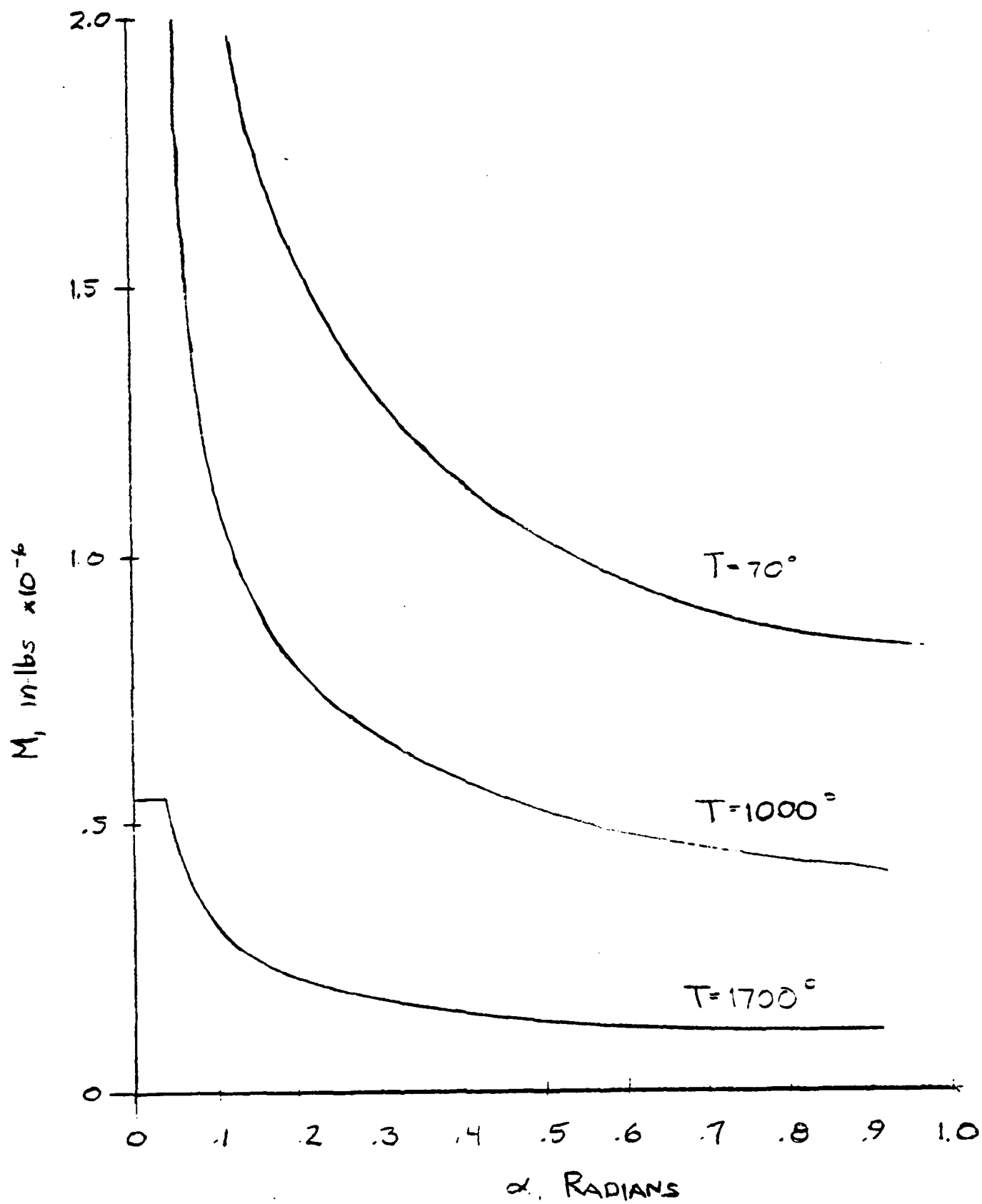
$$m_p = \frac{\sigma_{out}^2}{4} \quad (5.28)$$

The yield stress, and the maximum nominal flow stress as functions of temperature were determined in Chapter 5.

#### 5.1.5 The Final Form of the Hinge Moment

The analysis in the preceding section is not valid for the first phase of deformation. This phase will be approximated by assuming that for a moment greater than the fully plastic moment,  $M_o$ , is constant and equal to  $M_o$ . This would be a conservative assumption. For hinge angles greater than the jamming angle, Kecman offers the following formula:

$$M(\alpha) = M(\alpha_j) + 1.4[M - M(\alpha_j)](\alpha - \alpha_j) \quad (5.29)$$



RESULTS OF KECMAN'S ANALYSIS

FIGURE 5.5

This formulation has been programmed in a Microsoft-BASIC program. The source code is given in Appendix B. Figure 5.5 shows the results of the program.

### 5.2 Hayduk's and Wierzbicki's Method

The primary difference between Kecman's method and this method is that Hayduk and Wierzbicki considered not only inextensional deformation modes, but also extensional deformation patterns. The effect of these extensional modes will be fully developed in this section.

Hayduk's and Wierzbicki's formulation results in a closed form analytical solution which predicts the mean crushing force. Reference 11 specifically addresses the problem of analyzing the crushing process of thin walled, plate formed, open structures with particular emphasis on L shapes and cruciforms. The I beam can be approximated by two T shapes or four L shapes. Lower and upper bound solutions for the mean crushing strength of cruciforms was obtained by considering various modes of deformation. According to Hayduk and Wierzbicki, extensional deformation accounts for at least one third of the dissipated energy.

The end products of this section will include the application of Hayduk's and Wierzbicki's method to an I beam, and reviews of both references 11 and 12.

#### 5.2.1 Collapse Modes

Hayduk and Wierzbicki considered out of plane deformations in which the deflections exceed 10-100 times the section thickness and are of the order of magnitude of the web height and the flange width. The process of collapse starts as the compression flange loses stability, either elastically or plastically at a critical load,  $P_c$ . Following the buckling deformation, the flange can maintain added loads until a maximum load,  $P_{max}$ , is reached. Eventually, as the resistance decreases, the structure collapses completely. The structures being examined here often regain strength after the initial loss of resistance. Subsequent load peaks reveal the development of additional folds.

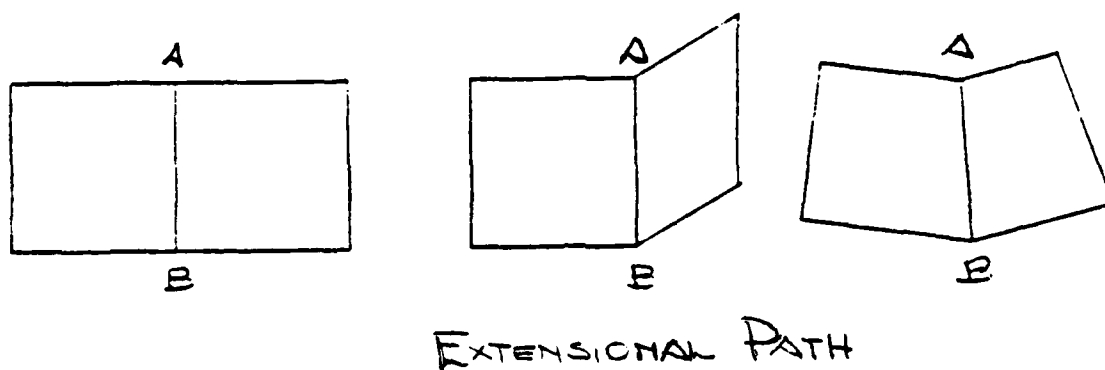
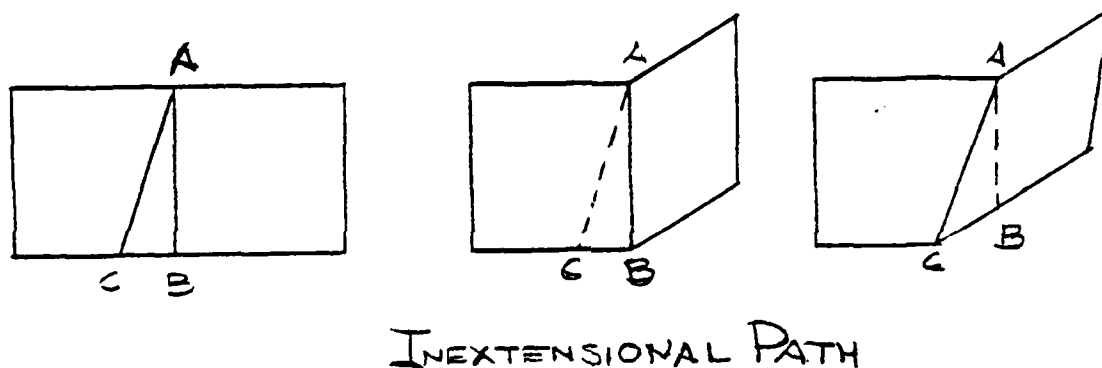
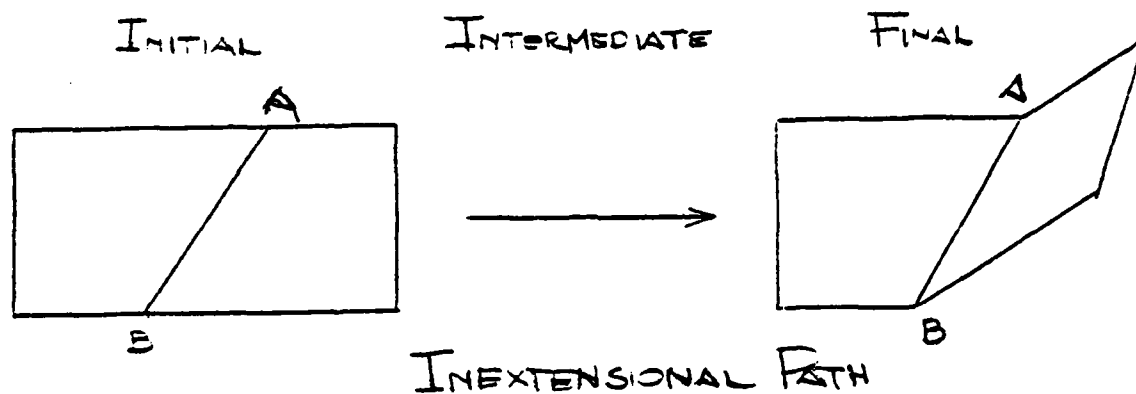
#### 5.2.1.1 Isometric Transformation Modes (Inextensional Deformations)

These modes are of the type used by Kecman to analyze the collapse mechanism. In this type of deformation, the energy is concentrated over hinge lines, while the rest of the structure remains rigid. An assumption of inextensional deformation is that material continuity is maintained. During the transformation of two surfaces, the lengths of corresponding arc elements is preserved. Hayduk and Wierzbicki show the progression of various deformation paths. These are illustrated in Figure 5.6.

In Figure 5.6 (a), and (b), the final state is formed inextensibly. This can only be done if the boundaries have sufficient freedom to deform. The element in Figure 5.6 (c) is initially folded along the stationary hinge line AB; finally the element is rotated extensibly, (ref. 11).

#### 5.2.1.2 Hinge Collapse Modes

There are two types of hinge collapse modes. The first is a propagating hinge line which occurs when the hinge line is free to move with respect to material points, and the



ILLUSTRATIONS OF INEXTENSIONAL AND  
EXTENSIONAL DEFORMATION PATHS

FIGURE 5.6

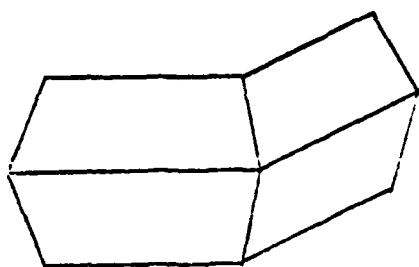


material of one flange is effectively transmitted to another flange. Extensional deformation occurs in the vicinity of the hinge line. This mode is a characteristic of thin walled structures consisting of two intersecting plates such as the I beam being considered in this study.

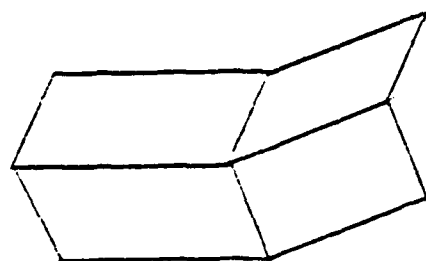
The second hinge collapse mode is the formation of a stationary hinge line. This mode is characterized by a hinge line fixed in the material. Side flanges which are initially rectangular are transformed into trapazoidal elements. Therefore, extension occurs over an entire flange. This mode will not be considered in this analysis, (ref. 11).

#### 5.2.1.3 Assembled Collapse Modes

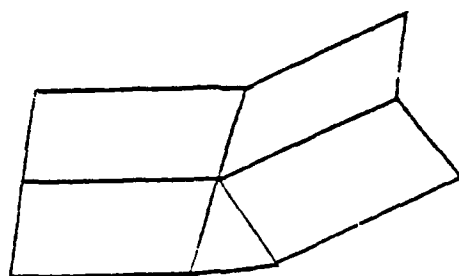
Hayduk and Wierzbicki demonstrated the method of assembling the folding patterns shown in Figure 5.6. The patterns are folded into more complicated symmetric, asymmetric and mixed collapse modes which are shown in Figure 5.7.



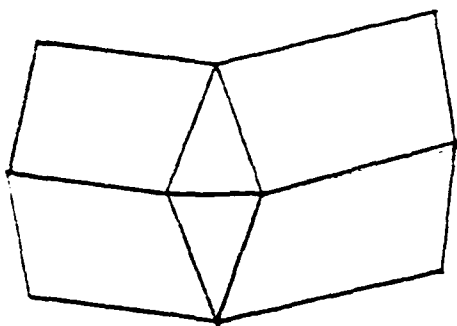
(a)



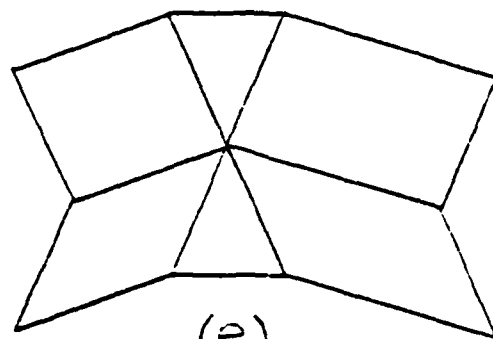
(b)



(c)



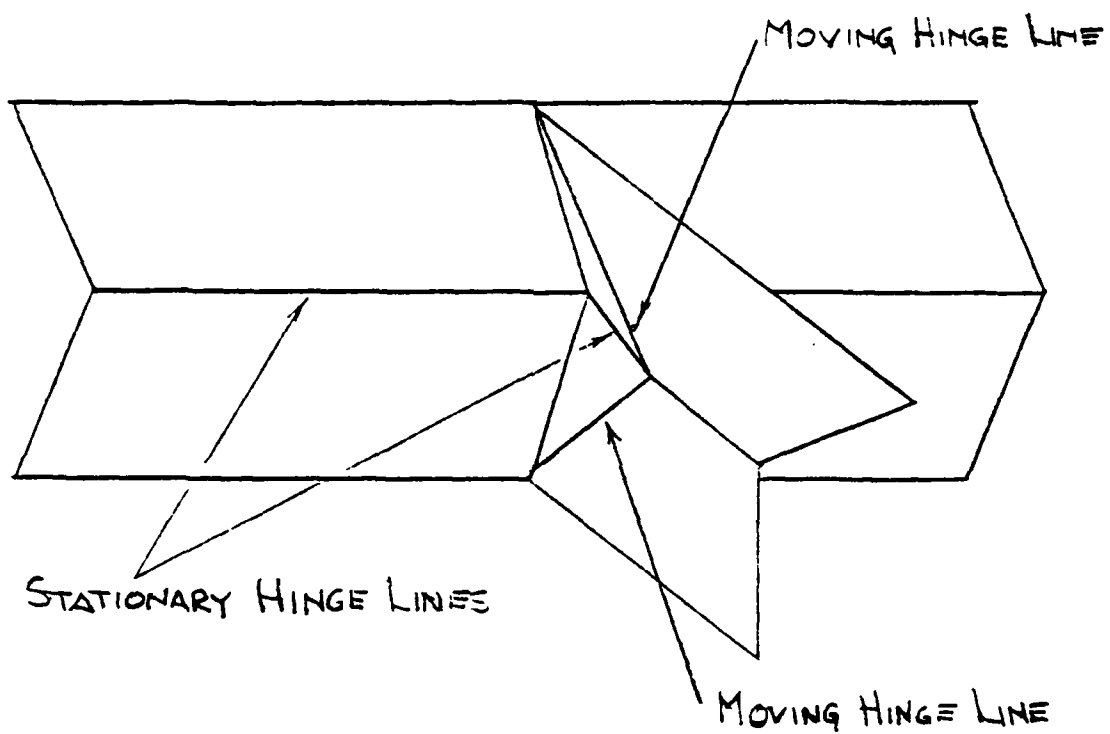
(d)



(e)

ASSEMBLING FOLDING MODES INTO  
MORE COMPLICATED PATTERNS

FIGURE 5.7



DEFORMATION PATTERN

FIGURE 5.8

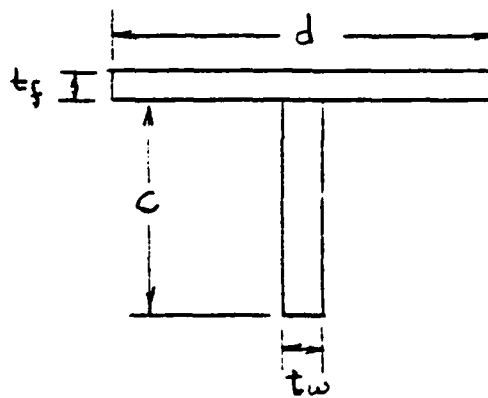
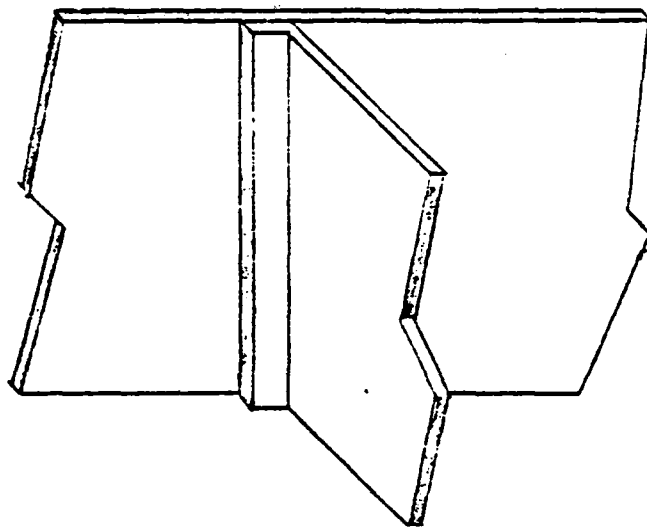
### 5.2.2 Analysis

For the purposes of this study, the analysis of a T section will be used; this analysis is considered to be equivalent to an I beam analysis. In reference 12, the short T cross section under consideration was subjected to compression with clamped boundary conditions. A model is presented in Figure 5.8.

For the purpose of estimating the mean crushing force,  $P_m$ , the T section is expanded into a plate and an angle as shown in Figure 5.9.

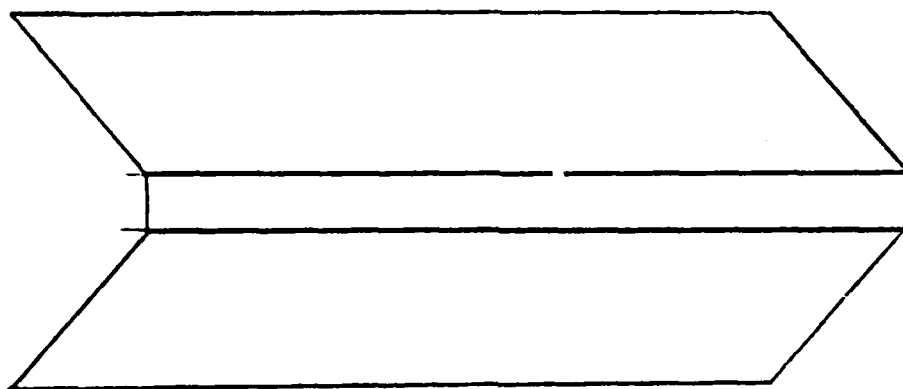
The plate will collapse through the bending zone limited by the two horizontal moving lines. The angle will follow the folding mechanisms described by Figure 5.10(b). The collapse modes in Figure 5.10(b) is consistent geometrically and kinematically. The regions are described as follows:

- (I) Four plane trapazoidal elements as rigid bodies.
- (II) Two sections of cylindrical surfaces at which continuous bending takes place without any extension.
- (III) Two sections of conical surfaces in which material is bent and rebent again as the material moves from one flange to another.

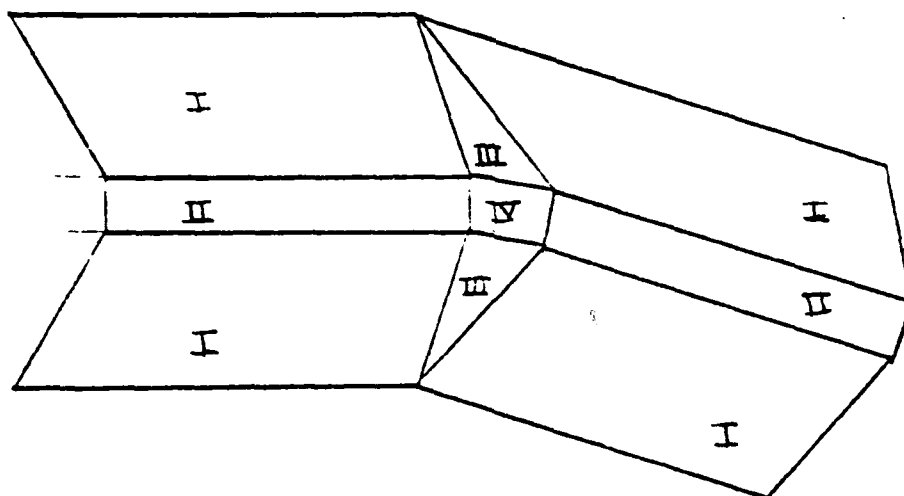


MODEL OF T SECTION

FIGURE 5.9



PLATE



ANGLE

FOLDING MECHANISMS

FIGURE 5.10

(IV) A section of toroidal surface which produces extension in a circumferential direction and continuously changes principal curvature in the other direction, (ref. 11)

The following assumptions will be used in this analysis:

- Neglect the short side of the angle element.
- The length of the two horizontal hinge lines is approximately equal to the length of the large side of the angle element.
- Two inclined hinge lines are of a length equal to a half wave length, H.
- The length of the toroidal surface in the vertical direction is neglected.

The energy dissipated of an angle element is given by summation of three terms, (ref 11):

1. The energy of a continuous deformation field in the section of a toroidal shell:

$$E_1 = 9.28 M_o H r / t_w \quad (5.30)$$

2. The energy dissipated by the discontinuous velocity

field in the horizontal hinge line of length,  $l$ :

$$E_2 = \frac{\pi}{2} M_o l \quad (5.31)$$

3. The work done by an inclined hinge line through the deformation process:

$$E_3 = 2.22 M_o H^2 / r \quad (5.32)$$

where:

$r$  = The small radius of the toroidal surface.

$M_o = \sigma_o [t_o]^2 / 4$ , the fully plastic yield moment per unit width

$H$  = Mode half-wave length

$\sigma_o = 0.7 \sigma_{ou}$

$\sigma_{ou}$  = Ultimate strength

$t_w$  = Web thickness

For the models given here:

$$2HP_m = E_1 + 4(E_2)_{web} + 4(E_2)_{flange} + 2E_3 \quad (5.33)$$

After substitution of the dissipated energies into (5.33):

$$P_m / M_o = 4.64 \frac{r}{t_w} + \frac{\pi}{H} \left[ c + d \left( \frac{t_f}{t_w} \right)^2 \right] + 2.22 \frac{H}{r} \quad (5.34)$$



Optimizing equation (5.34) by using the following partial derivatives:

$$\frac{\partial P_m}{\partial r} = 0 \quad (5.35a)$$

$$\frac{\partial P_m}{\partial H} = 0 \quad (5.35b)$$

Equating (5.35a) and (5.35b) yields:

$$r = \left[ \frac{2.22}{4.64^2} \pi t_w^2 \left( c + d \left( \frac{t_f}{t_w} \right)^2 \right) \right]^{1/3} \quad (5.36)$$

$$H = \left[ \frac{\pi^2 t_w}{(2.22)(4.64)} \left( c + d \left( \frac{t_f}{t_w} \right)^2 \right) \right]^{1/3} \quad (5.37)$$

Ultimately, the three basic mechanisms of energy dissipation appear equally weighted in the final equation for mean crushing force:

$$P_m/M_o = 3 \left[ (4.64)(2.22)\pi \left( 1 + k \left( \frac{t_f}{t_w} \right)^2 \right) \left( \frac{c}{t_w} \right) \right]^{1/3} \quad (5.38)$$

Equation (5.38) may be simplified as follows:

$$P_m/M_o = 3[A_1 A_2 A_3 \left( \frac{c}{t_w} \right)]^{1/3} \quad (5.39)$$

where:

$$k = \frac{d}{c} \quad (5.40)$$

$$A_1 = 4.64 \quad (5.41)$$

$$A_2 = \pi \left[ 1 + k \left( \frac{t_f}{t_w} \right)^2 \right] \quad (5.42)$$

$$A_3 = 2.22 \quad (5.43)$$

Note also that equations (5.34), (5.36), and (5.37) may be

simplified into the following forms:

$$P_m/M_o = A_1 \frac{r}{t_w} + A_2 \frac{c}{2H} + A_3 \frac{H}{3r} \quad (5.44)$$

$$r = [(A_2 A_3 / A_1^2) (c t_w^2)]^{1/3} \quad (5.45)$$

$$H = [(A_2^2 / A_1 A_3) (c^2 t_w^2)]^{1/3} \quad (5.46)$$

The application of these equations to the case of an I beam requires that the geometric parameters be modified. An I beam is two T sections, hence the dimensions are doubled; but,  $b = 2c$ , which yields the following relations.

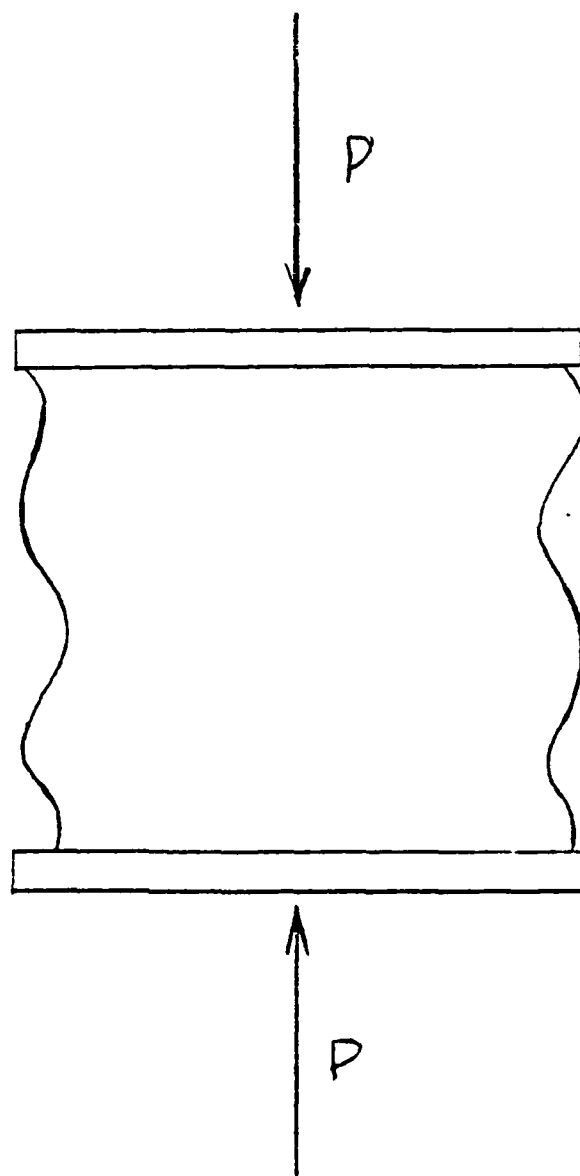
$$P_m/M_o = 3[A_1 A_2 A_3 (b/2t_w)]^{1/3} \quad (5.47)$$

$$k = 2a/b \quad (5.48)$$

It is now possible to apply this relation determined for the crushing case to the bending case. The geometry of this crushing mode is given in Figures 5.11 and 5.12.

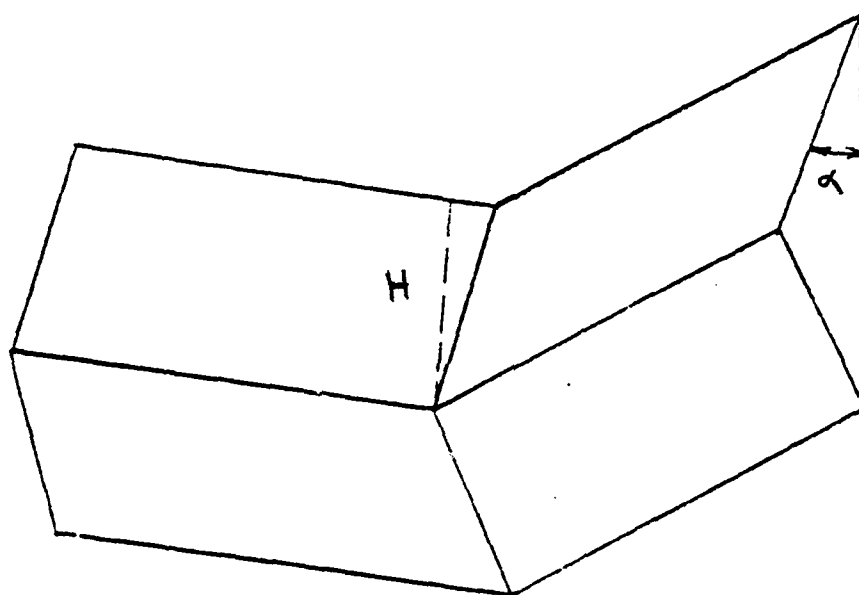
Recall the propagating hinge line mode as described in paragraph 5.2.1.2. This mode describes the global geometry of the crushing process and is determined purely by the width of the two side panels,  $d$ , which is prescribed, the wavelength,  $H$ , which is to be determined, and the crushing rotation angle,  $\alpha$ , which is a parameter of the process. The relation between the axial displacement,  $\delta$ , and the angle,  $\alpha$ , is:

$$\delta = 2H(1 - \cos\beta) \quad (5.49)$$



CRUSHING CASE

FIGURE 5.11



EXTENSIONAL COLLAPSE MODE -  
DEFINITION OF GEOMETRIC PARAMETERS

FIGURE 5.12

Reference 12 determined an expression for the instantaneous crushing force,  $P$ , normalized with respect to  $P_m$ :

$$P/P_m = \frac{1}{3} [2\cos\beta + \frac{2}{\pi\sin\beta} + \frac{0.9\cos\beta}{\tan\beta(1 + \sin^2\beta)^{1/2}}] \quad (5.50)$$

Figure 5.13 gives the geometry of the bending case. From Figure 5.13:

$$\tan\frac{\alpha}{2} = \frac{\delta/2}{b} \quad (5.51)$$

Thus, it may be said that:

$$P/P_m = f(\delta) = f(2b\tan\frac{\alpha}{2}) \quad (5.52)$$

For a section width,  $b$ :

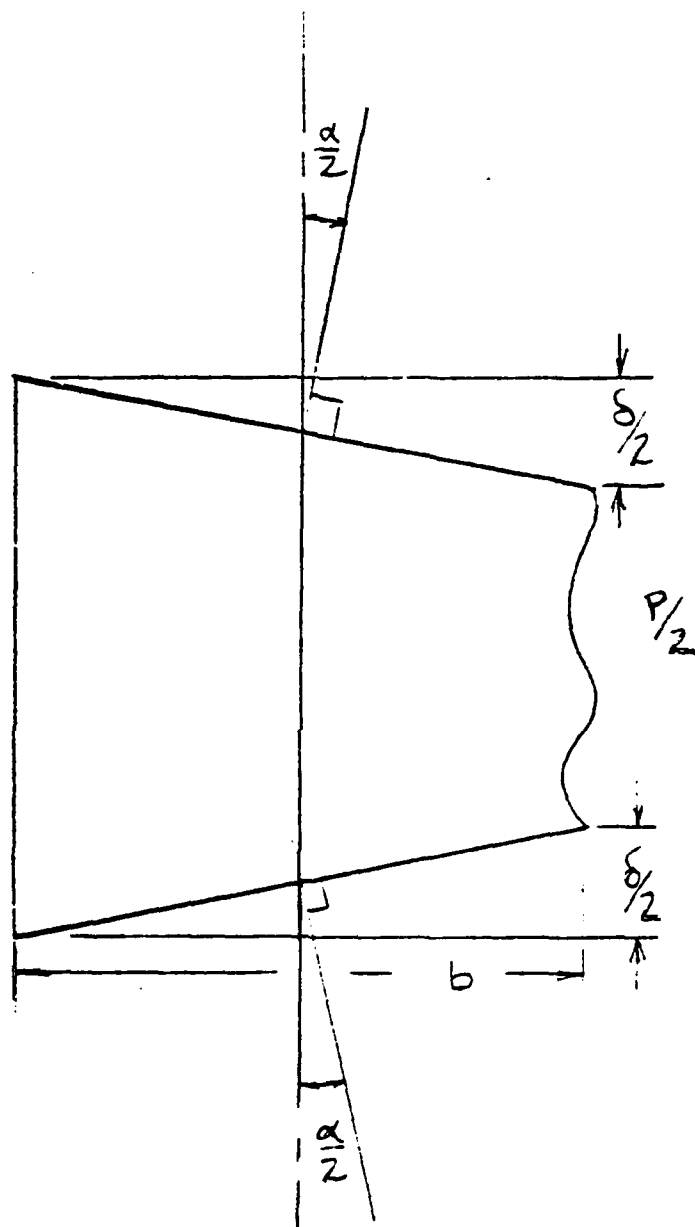
$$M = \frac{P}{2} b \quad (5.53)$$

$$M_m = \frac{P_m}{2} b \quad (5.54)$$

Where  $M$  is the mean moment due to bending rotation,  $\alpha$ , as defined in Figure 5.14. After equating (5.53), and (5.54):

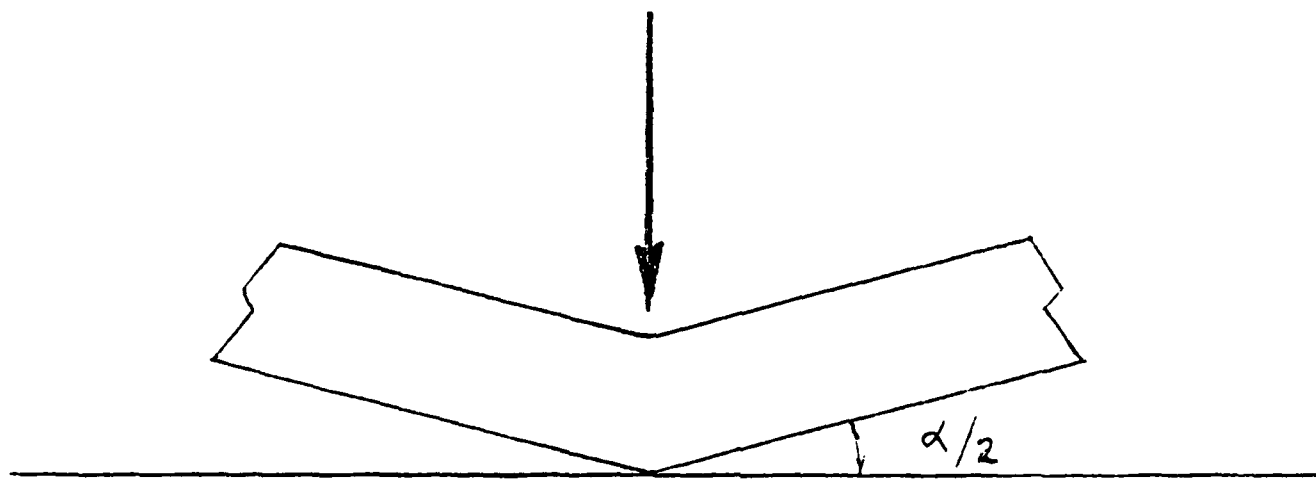
$$\frac{M}{M_m} = \frac{P}{P_m} \quad (5.55)$$

Figure 5.15 gives  $P/P_m$  as a function of  $\delta/2H$  based on equations (5.49), and (5.50), (ref. 12). This graph is an equivalent description of  $M/M_m$  as a function of  $(b/H)[\tan(\alpha/2)]$ .



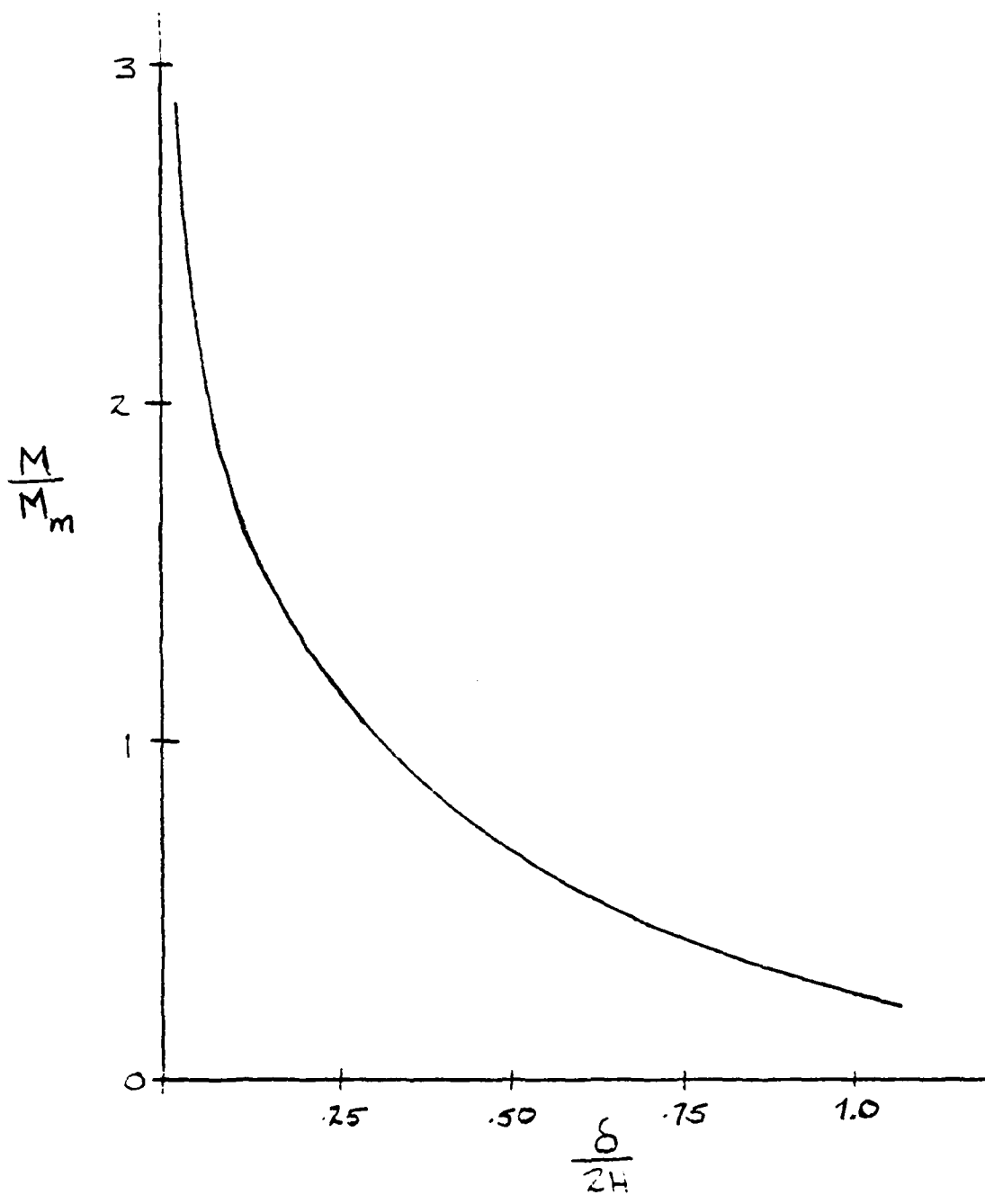
BENDING CASE

FIGURE 5.13



DEFINITION OF ANGLE OF ROTATION

FIGURE 5.14



MOMENT DISPLACEMENT RELATION

FIGURE 5.15



For this purposes of this study, an approximate relation for  $M/M_m$  and  $\alpha$  will be determined. Assume equation (5.56) is a valid function for  $M/M_m$  :

$$M/M_m = D/(\delta/2H)^n \quad (5.56)$$

where:

$D, n$  are constants

Assume the new curve goes through points  $P_1$ , and  $P_2$ , in Figure 5.15.

$$P_1(\delta/2H, M/M_m) = (0.30, 1.0) \quad (5.57)$$

$$P_2(\delta/2H, M/M_m) = (1.0, 0.24) \quad (5.58)$$

Solving for  $D, n$ :

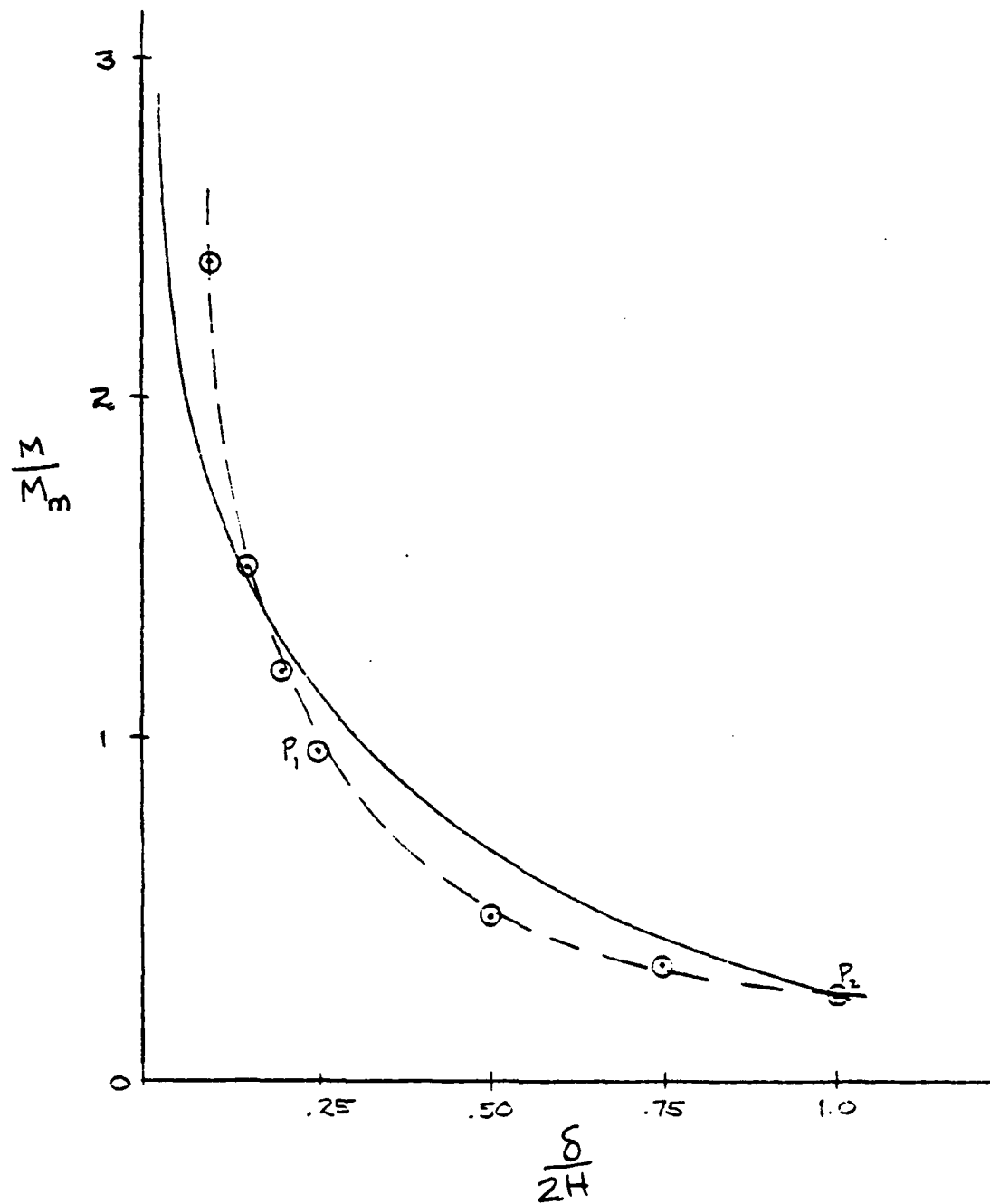
$$D = 0.24 \quad (5.59)$$

$$n = 1.2 \quad (5.60)$$

Assuming  $n = 1.0$ , the following equation results:

$$M/M_m = \frac{0.24}{\delta/2H} \quad (5.61)$$

Figure 5.16 shows how the approximate solution compares to the exact solution. Substituting equation (5.51) into equation (5.61), the following results:



COMPARISON OF APPROXIMATE  
AND EXACT SOLUTIONS

FIGURE 5.16

$$M/M_m = \frac{0.24}{(b/H) \tan(\alpha/2)} \quad (5.62)$$

Considering equation (5.54):

$$M = \frac{P_m b}{2} \left[ \frac{0.24}{(b/H) \tan(\alpha/2)} \right] \quad (5.63)$$

Now substitute equation (5.47) into (5.63)

$$M = [3M_o [A_1 A_2 A_3 (b/2t_w)]^{1/3}] [b/2] \left[ \frac{0.24 H}{b \tan(\alpha/2)} \right] \quad (5.64)$$

But  $M_o$  is the fully plastic yield moment for the flange

$$M_o = \frac{\sigma_o t^2}{4} \quad (5.65)$$

where  $t = t_f = t_w$

The desired final result of this analysis is a relation between  $M$  and  $M_o$ . Rewriting equation (5.65):

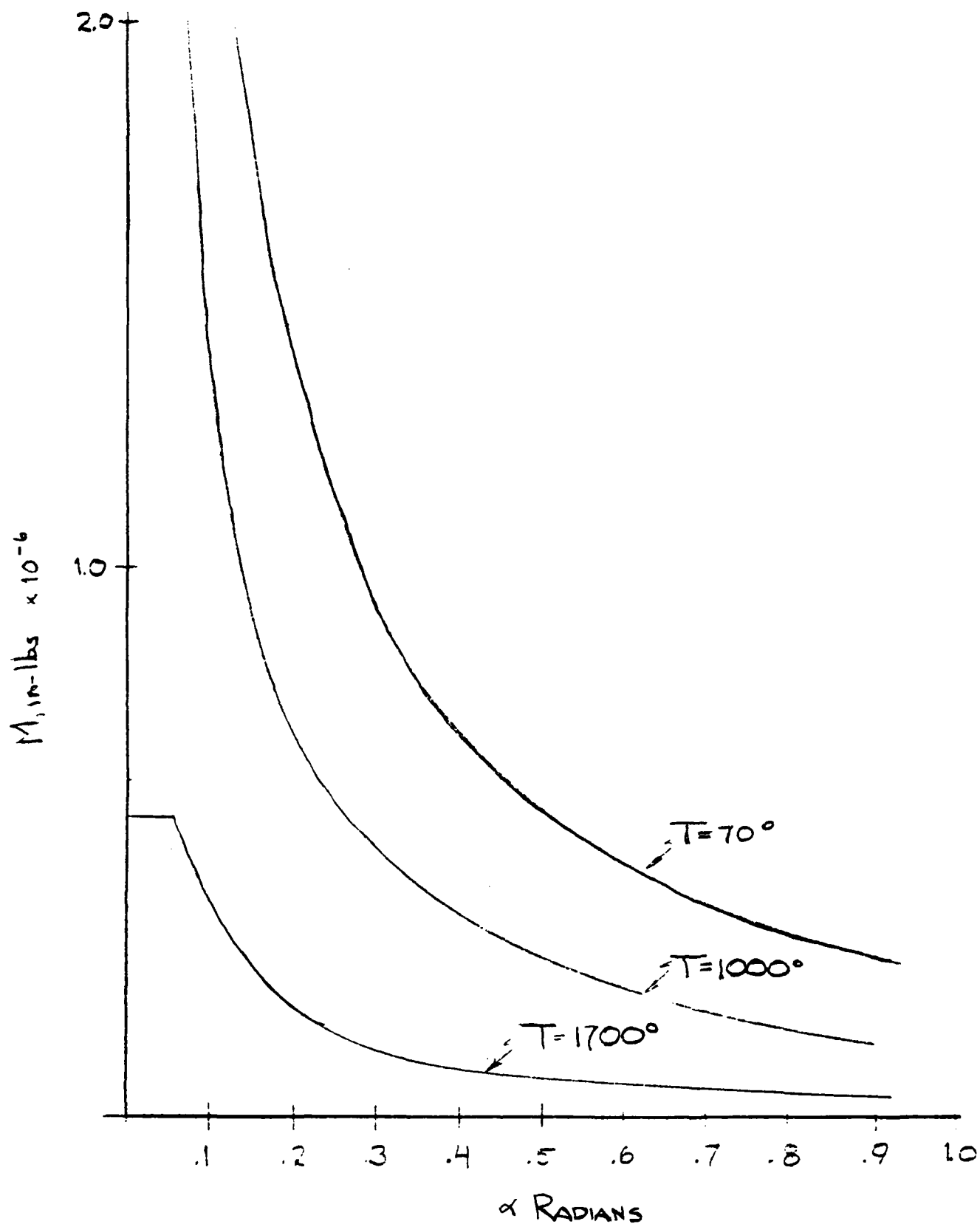
$$M_o' = \sigma_o \int_A z dA \quad (5.66)$$

Recall equations (2.2) and (2.4):

$$\sigma_o(T) = -20.5T + 40,000.0 \quad (2.2)$$

$$\int_A z dA = abt + \frac{b^2 t}{4} \quad (2.4)$$

Finally, substitute equation (2.4), (5.66), (5.65), and (5.46) into (5.64):



$\alpha$  RADIANS  
RESULTS OF HAYDUK AND  
WIERZBICKI'S ANALYSIS  
FIGURE 5.17

$$M/M_o' = \frac{3\sigma_o t^2}{4\sigma_o (abt + b^2 t/4)} [A_1 A_2 A_3 (b/2t)]^{1/3} \left(\frac{b}{2}\right) \left[ \frac{0.24 [(A_2^2/A_1 A_3) b^2 2t]^{1/3}}{b \tan(\alpha/2)} \right]$$

The simplified final result of this relation is:

$$M/M_o' = \frac{0.36\pi t (b + 2a)}{\tan(\alpha/2) [b(b + 4a)]} \quad (5.68)$$

Figure 5.17 shows graphically the resulting moment-angle rotation relationship as determined by Hayduk and Wierzbicki. Appendix C contains the source code for a Microsoft BASIC program which determines the moments resulting from equation (5.72).

### 5.3 Comparison of Results of the Two Methods

The primary difference between the two methods of analyses is that Kecman considered only inextensional deformation modes, whereas Hayduk and Wierzbicki considered extensional deformations as well as inextensional deformation. Since the second method considered more energy dissipation than the first, the allowable moments due to deformation are greater. However, for angles greater than one tenth of the jamming angle, Kecman's method yields greater moments. The errors induced by his numerical integration

technique are compounded as the angles increase. Figure 5.18 shows graphically how the results of each analysis differs. The dimensions of the section analyzed are given below:

$$a = 12 \text{ inches}$$

$$b = 12 \text{ inches}$$

$$t_f = t_w = .6 \text{ inches}$$

The maximum moment given in Figure 5.18 is the fully plastic yield moment of the section, hereafter called  $M_o$ , which is only a function of geometry and temperature of exposure of the beam. Hence,  $M_o$  is not a function of the analysis method.

Clearly, as the angle of rotation increases the moment decreases; and as the temperature increases, the moment decreases. Appendices B and C also contain results which show the effects of changing the geometry of the section. For both analyses, the moments are decreased as the section thickness decreases; the web height decreases; or the flange width decreases.

These methods of analyses are considered accurate predictions of the failure mechanisms of a beam exposed to fire. Recommendations for using the information provided by these analyses will be given in the following chapter.

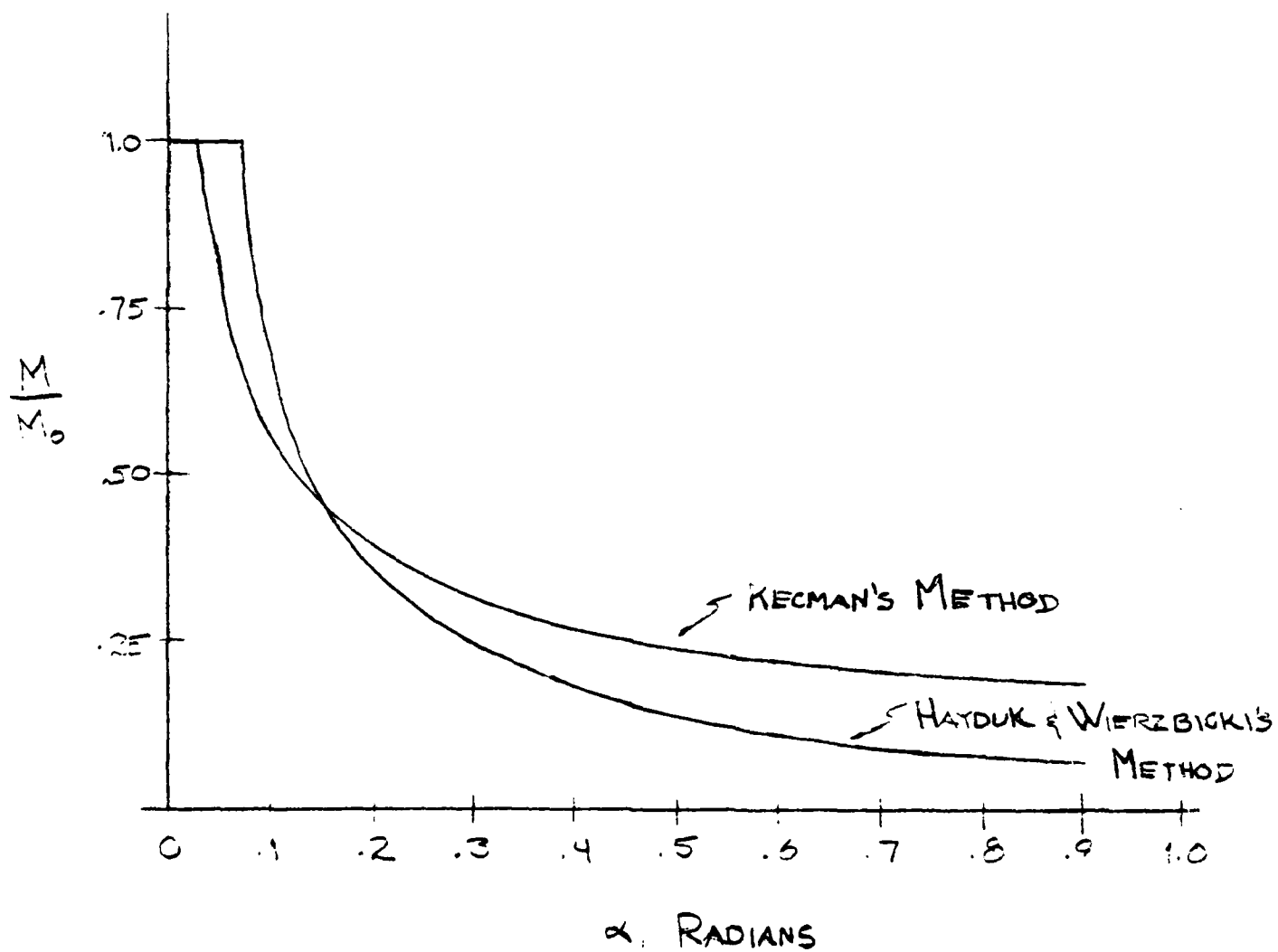


FIGURE 5.18

## Chapter 6

### CONCLUSIONS AND RECOMMENDATIONS

A summary of each chapter is presented here with concluding remarks. Finally, recommendations are offered for using this analysis for future studies.

#### 6.1 Summary

As stated in the introduction, the ultimate objective of this study was to show how much the strength of a shipboard structural member is diminished when exposed to fire. To this end, Chapters 2, 3, and 4 provided input into the analyses of the failure mechanisms studied in Chapter 5. The results of the preceding chapters will be summarized here.

Chapter 2 developed the model of the structure. Simple observations revealed that the ship is a redundant structure composed of beams, plates, and columns. The motivation towards choosing an I beam for the analysis was developed.



The material selected for the model was ASTM-A36 steel as its physical and mechanical properties are similar to the properties of ABS Grade A steel, a common shipbuilding steel. The equations for the temperature dependent mechanical properties were the output of this chapter to be used in the analysis.

Chapter 3 provided background for characterizing shipboard fires. Three parameters which are assumed to be accurate predictions of the contributing factors of a fully developed fire were defined. These factors are: the duration of the fully developed fire; the overall penetration flux; and the average fire temperature. Since fire is indeed a complex process with several unquantifiable variables, a time temperature curve was used as a definition of the fire process. For the purposes of this study, a step function to 1700<sup>o</sup> F was used as the time temperature relation.

Chapter 4 was the heat transfer analysis which determined the relationship between the elevated temperature exposure and the distance along the length of the beam. The results of this analysis led to the conclusion that a beam exposed to fire will experience the same failure mechanisms as a beam under a point load.

Finally, the primary thrust of this study was to analyze

the failure mechanisms due to fire exposure. Two methods were fully developed in the preceding chapter and the results were summarized graphically in Figure 5.18.

## 6.2 Recommendations

The ultimate objective of any structural design process is to develop a structure which is strong enough to withstand all expected service loads and a high percentage of unexpected loads. The information provided by the analysis in Chapter 5 is considered useful input for the design of shipboard structures. It is possible through the use of Figure 5.18 to determine how the stiffness of a structural member is decreased when exposed to elevated temperatures. The diminished stiffnesses may be used as input to a finite element program which simulates a ship structure. The effect of a shipboard fire upon the entire structure may then be determined.

The examination of the effect that one weakened member has on the other members of a redundant structure is considered fertile ground for future studies. Reference 16 may provide insight into the behavior of this phenomenon. Zubelewicz and Mroz numerically simulated rock burst processes

AD-A144 810

ANALYSIS OF THE FAILURE MECHANISM OF SHIPBOARD  
STRUCTURAL MEMBERS EXPOSED TO FIRE(U) MASSACHUSETTS  
INST OF TECH CAMBRIDGE DEPT OF OCEAN ENGINEERIN.

2/2

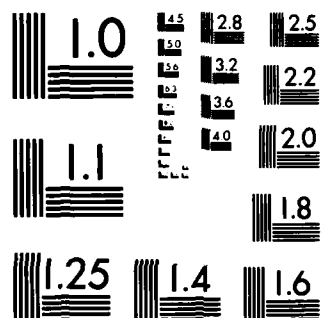
UNCLASSIFIED

R L HIDDEN JUN 84 N66314-70-A-0013

F/G 13/13

NL





MICROCOPY RESOLUTION TEST CHART  
NATIONAL BUREAU OF STANDARDS-1963-A

treated as problems of dynamic instability. According to reference 16, local plastic failure occurs at one location (such as in a member of a ship's structure) and the elastic energy flows to the hinge and is the driving force into the damage. Energy then flows into the neighboring hinges, which is to say that one unstable member may produce a chain reaction and other members may subsequently fail.

As a final word, it is highly recommended to utilize the information provided in this study as an aid for examining the effect of fires on the ship's structure. Ultimately a ship may be designed to withstand shipboard fires.

## REFERENCES

1. McCarthy, F., The Behavior of Structural Elements Exposed to Fire, Massachusetts Institute of Technology, Department of Ocean Engineering, Ocean Engineer's thesis, 1981.
2. Harmathy, T.Z., and Stanzak, W.W., "Elevated Temperature Tensile and Creep Properties of Some Structural and Prestressing Steels", Fire Test Performance, ASTM Special Technical Publication 464, American Society for Testing and Materials, Philadelphia, 1970.
3. Harmathy, T.Z., "Design to Cope with Fully Developed Fires", Design of Buildings for Fire Safety, ASTM Special Technical Publication 685, American Society for Testing and Materials, Philadelphia, 1977.
4. "Aluminum Fire Protection Guidelines", Technical and Research Bulliten, 2-21, Society of Naval Architects and Marine Engineers, New York, 1974.
5. "ASTM Fire Tests of Building Construction and Materials (E119)", American Society for Testing and Materials, Philadelphia.
6. Correspondence with Marchand, A., Department of Navy, Naval Sea Systems Command, SEA 55X23/AM, Ser 47, 27 January 1984.
7. Rohsenow, W.M., and Choi, H., Heat Mass and Momentum Transfer, Prentice-Hall, Englewood Cliffs, N.J., 1961.

8. Hildebrand, F.B., Advanced Calculus for Applications, Prentice Hall, Englewood Cliffs, N.J., 1976.
9. Masubuchi, K., "Analysis of Welded Structures", International Series on Material Science and Technology, Volume 33, Pergamon Press, New York, 1980.
10. Kecman, D., "Bending Collapse of Rectangular and Square Section Tubes", International Journal of Mechanical Science, Volume 25, Number 9-10, 1983.
11. Hayduk, R.J., and Wierzbicki, T., "Extensional Collapse Modes of Structural Members", Computers and Structures, Volume 18, Number 3, 1984.
12. Wierzbicki, T., "On the Formation and Growth of Folding Modes", Collapse, Cambridge University Press, 1983.
13. Zubelwicz, A., and Mroz, Z., "Numerical Simulation of Rock Burst Processes Treated as Problems of Dynamic Instability", Rock Mechanics and Rock Engineering, Volume 16, 1983.

## Appendix A

### HEAT TRANSFER ANALYSIS PROGRAM

```
10 REM PROGRAM TO CALCULATE TEMPERATURE GRADIENT IN A BEAM
20 DIM TEMP(20),Y(20),Z(20),TOP(20)
25 INPUT "ENTER THE BEAM LENGTH IN FEET";XL
30 INPUT "IS BEAM SOLID (S) OR I (I)";N$
40 IF N$="I" THEN GOTO 90
45 LPRINT " SOLID BEAM"
50 INPUT "ENTER WIDTH OF BEAM";W
60 INPUT "ENTER DEPTH OF BEAM";D
65 LPRINT " WIDTH, DEPTH="; W;D
70 B=SQR((12/5.4)*((1/D)+(1/W)))
80 GOTO 155
84 LPRINT " I BEAM"
90 INPUT "ENTER WIDTH OF FLANGE";W
100 INPUT "ENTER DEPTH OF WEB";D
105 LPRINT " WIDTH OF FLANGE, DEPTH OF WEB="; W;D
110 INPUT "ENTER THICKNESS OF FLANGE";T1
120 INPUT "ENTER THICKNESS OF WEB";T2
125 LPRINT " THICKNESS OF FLANGE, THICKNESS OF WEB=";T1;T2
130 P=2*(D+2*W+2*T1-T2)
140 S=2*(T1*W)+(D*T2)
150 B=SQR((12/5.4)*(P/S))
155 LPRINT " LENGTH OF BEAM=";XL;" FEET"
156 LPRINT " B=";B : LPRINT " "
```



```

160 BL=B*XL
170 BOT=EXP(BL)-EXP(-BL)
180 X=XL/20
190 LPRINT " PT NO X T-Ta/Tb-Ta"
200 FOR K%=1 TO 20
210 Y(K%)=X*K%
220 Z(K%)=B*(XL-Y(K%))
230 TOP(K%)=EXP(Z(K%))-EXP(-Z(K%))
240 TEMP(K%)=TOP(K%)/BOT
250 LPRINT " ";K%,Y(K%),TEMP(K%)
260 NEXT K%
270 END

```

## Appendix B

### KECMAN'S ANALYSIS PROGRAM

```
10 DIM W(20)
20 INPUT "TEMPERATURE OF EXPOSURE, DEGREES F";T
30 INPUT "FLANGE WIDTH, INCHES";A
40 INPUT "WEB HEIGHT, INCHES";B
41 INPUT "THICKNESS, INCHES";TH
42 LPRINT " "
50 LPRINT " "
51 LPRINT " TEMPERATURE=";T
52 LPRINT " FLANGE WIDTH=";A
53 LPRINT " WEB HEIGHT=";B
54 LPRINT " THICKNESS=";TH
60 S0=-20.5*T+40000.0
65 IF T>=1951 THEN S0=4.5
67 M0= S0*B*TH*(A+B/4)
68 LPRINT " FULLY PLASTIC MOMENT, INCH-POUNDS";M0
70 J=0
90 U=3.14159265
100 IF A <= B THEN H=A/2
110 IF A > B THEN H=B/2
120 Q1=(H-.5*TH)/B
130 D=2*(ATN(Q1/SQR(-Q1*Q1+1)))
131 LPRINT " JAMMING ANGLE, RADIANS";D
132 LPRINT " ANGLE; MOMENT/M0; MOMENT"
```

```

140 X=SU*(TH^2)/4
150 FOR K=D/10 TO 11*D/10 STEP D/10
151 P1 = K/2-K^3/48+K^5/3840
152 P2 = 1-K^2/8+K^4/384
153 P3 = B*P1
154 P4 = (2*H - P3)
155 P5 = B*P2
156 P6 = H*P1
157 P7 = P1/P2
165 YB = P5-(SQR(P3*P4))
170 R=(.07-K/70)*H
180 ZA=(P3*P1)-P6+(SQR(P3*P4))*P2
190 Q1=1-(B/H)*P1
200 Q2=ATN(Q1/SQR(-Q1*Q1+1))
210 W1=2*A*(U/2-K/2-Q2)
220 W2=A*(U-2*Q2)
230 W3=(P3*P1-P6+(SQR(P3*P4))*P2)*(U-2*Q2)
240 W4=H*U
250 YC=(H*P7+P5-(SQR(P3*P4)))/(1+P7^2)
260 XC=YC*P7
270 Q1=ZA/(SQR(((H-XC)^2)+((YC-YB)^2)))
280 Q3=ATN(Q1)
290 W5=2*B*Q3
300 W7=4/3*(ZA/R)*(SQR((H^2)+(YB^2)+(ZA^2)))
310 W6=2*(H/R)*ZA
320 Q1=ZA/YB
330 Q3=ATN(Q1)

```

```

340 W8=2*(A*(K/2)+2*H*Q3)
350 J=J+1
360 W(J)=W1+W2+W3+W4+W5+W6+W7+W8
370 NEXT K
380 FOR I%=1 TO J-1
390 Y=(TH/(B*(4*A+B)))*(W(I%+1)-W(I%))/(D/10)
391 M1=Y*M0
400 LPRINT " ";I%*D/10;Y;M1
401 NEXT I%
402 LPRINT " "
403 LPRINT " "
404 LPRINT " "
410 LPRINT " "
420 END

```

## Appendix C

### HAYDUK AND WIERZBICKI'S ANALYSIS PROGRAM

```
10 INPUT "TEMPERATURE OF EXPOSURE, DEGREES F";T
30 INPUT "FLANGE WIDTH, INCHES";A
40 INPUT "WEB HEIGHT, INCHES";B
50 INPUT "THICKNESS, INCHES";TH
61 LPRINT " "
62 LPRINT " "
70 LPRINT " TEMPERATURE ";T
80 LPRINT " FLANGE WIDTH";A
90 LPRINT " WEB HEIGHT";B
100 LPRINT " THICKNESS";TH
120 T1=(A*B*TH+B*B*TH/4)
130 T2=-20.5*T+40000
135 IF T>=1951 THEN T2=4.5
137 M0=T2*T1
138 LPRINT " FULLY PLASTIC MOMENT, INCH-POUNDS";M0
140 T3=0.36*3.141593*TH*(B+2*A)
150 T4=1/(B*(B+4*A))
170 LPRINT" ANGLE; MOMENT/M0; MOMENT"
171 IF A<=B THEN J=A/2
172 IF A>B THEN J=B/2
175 Q1=(J-.5*TH)/B
176 D=2*(ATN(Q1/SQR(-Q1*Q1+1)))
180 FOR K=D/10 TO D STEP D/10
```

```
181 T5=TAN(K/2)
190 M=T3*T4/T5
195 M1=M*M0
200 LPRINT " ";K;M;M1
201 NEXT K
202 LPRINT " "
203 LPRINT " "
204 LPRINT " "
210 LPRINT " "
220 END
```

END

FILMED